

©2018. American Geophysical Union. All Rights Reserved. Access to this work was provided by the University of Maryland, Baltimore County (UMBC) ScholarWorks@UMBC digital repository on the Maryland Shared Open Access (MD-SOAR) platform.

Please provide feedback Please support the ScholarWorks@UMBC repository by emailing [scholarworks-group@umbc.edu](mailto:scholarworks-group@umbc.edu) and telling us what having access to this work means to you and why it's important to you. Thank you.

# JGR Space Physics

## RESEARCH ARTICLE

10.1029/2020JA028710

### Key Points:

- Total electron content profiles of the Io plasma torus from Juno Perijoves 10, 11, 14, and 15
- The locations of Io plasma torus regions depend on longitude as expected
- Factors that control scale heights and peak total electron contents are not yet determined

### Correspondence to:

P. H. Phipps,  
[phipps@umbc.edu](mailto:phipps@umbc.edu)

### Citation:

Phipps, P. H., Withers, P., Buccino, D. R., Yang, Y.-M., & Parisi, M. (2021). Two years of observations of the Io plasma torus by Juno radio occultations: Results from Perijoves 1 to 15. *Journal of Geophysical Research: Space Physics*, 126, e2020JA028710. <https://doi.org/10.1029/2020JA028710>

Received 13 SEP 2020

Accepted 22 JAN 2021

## Two Years of Observations of the Io Plasma Torus by Juno Radio Occultations: Results From Perijoves 1 to 15

Phillip H. Phipps<sup>1</sup> , Paul Withers<sup>2</sup> , Dustin R. Buccino<sup>3</sup> , Yu-Ming Yang<sup>3</sup> , and Marzia Parisi<sup>3</sup> 

<sup>1</sup>University of Maryland, Baltimore County, Baltimore, MD, USA, <sup>2</sup>Department of Astronomy, Boston University, Boston, MA, USA, <sup>3</sup>Jet Propulsion Laboratory, California Institute of Technology, Pasadena, CA, USA

**Abstract** The Io plasma torus is the primary source for plasma in Jupiter's magnetosphere. Observations of fundamental properties of the torus place valuable constraints on how the Io plasma torus behaves. Yet measurements of the density structure of the torus that precisely determine its location, total electron content, and scale height are rare. Here, we report measurements of four profiles of the total electron content through the torus by the Juno spacecraft. These profiles were acquired by radio occultation observations during Juno Perijoves 10, 11, 14, and 15. They complement previously reported profiles from Perijoves 1, 3, 6, and 8, for which an initial ad hoc correction has been verified by improved calibration at the ground station. Fits to each profile determined the location, peak total electron content, and scale height of two torus regions: the cold torus and the torus beyond 5.5  $R_J$ . Measurements show the torus locations depend on longitude, but not time. The peak total electron content values vary with time but do not exhibit any clear dependence on longitude. The scale heights may depend on longitude and/or time. There is no apparent dependence of these properties on the Io phase angle. Future analysis of more observations by the Juno spacecraft will clarify the respective roles of longitude, time, and the Io phase angle in shaping the density structure of the Io plasma torus. Observations at previously sampled longitudes will be particularly valuable, as demonstrated here by Perijoves 8 and 15, which sampled the same longitude 1 year apart.

## 1. Introduction

The innermost Galilean satellite, Io, is the source of most of the material in Jupiter's magnetosphere. This material, made mostly of sulfur and oxygen atoms, gets ionized and trapped by Jupiter's magnetic field (Thomas et al., 2004). The ionized material is transported radially through the magnetosphere. The plasma is then lost via charge exchange with neutrals or transported to the outer magnetosphere. The highest density of the plasma lies between 5 and 10  $R_J$  in what is called the Io plasma torus (IPT).

The plasma trapped in the IPT is distributed into three distinct regions: the cold torus, ribbon, and warm torus (Bagenal, 1994; Bagenal & Sullivan, 1981; Thomas et al., 2004). Each region has a distinct temperature and composition (Bagenal, 1994; Bagenal & Sullivan, 1981; Bagenal, Adriani, et al., 2017; Nerney et al., 2017; Schneider & Trauger, 1995; Schneider et al., 1997; Steffl et al., 2006, 2008; Thomas et al., 2004). The cold torus is centered around 5.2  $R_J$ , contains mostly  $S^+$  ions with lesser amounts of  $O^+$  ions, has peak densities around 1,000  $cm^{-3}$ , ion temperatures around 2–4 eV, and a scale height  $\sim 0.1 R_J$ . The cold torus is thought to form by rapid radiative cooling of ions that diffuse toward Jupiter. The ribbon is centered around 5.6  $R_J$ , contains mostly  $O^+$  ions with lesser amounts of  $S^+$  ions, has peak densities around 3,000  $cm^{-3}$ , has ion temperatures around 10–30 eV, and a scale height of  $\sim 0.6 R_J$ . The ribbon is visible as a narrow region of bright  $S^+$  emissions in ground-based observations at optical wavelengths. The warm torus has maximum densities at 5.9  $R_J$  (Io's orbital distance) but extends outwards to  $\sim 8 R_J$  (approaching Europa's orbit). It contains mostly  $S^{2+}$  and  $O^+$  ions, has peak densities around 2,000  $cm^{-3}$ , has ion temperatures around 60 eV, and a scale height  $\sim 1.0 R_J$ . The warm torus region contains most of the plasma in the IPT. Previous observations have shown temporal and spatial variability in the torus by up to 50 percent (Herbert et al., 2008; Nozawa et al., 2004, 2005, 2006; Schneider & Trauger, 1995; Schneider et al., 1997; Steffl, Stewart, & Bagenal, 2004a; Steffl, Delamere, & Bagenal, 2004b; Steffl et al., 2006, 2008; Tsuchiya et al., 2015; Tsuchiya et al., 2019; Yoneda et al., 2009, 2010, 2013).

In the absence of rotation, the Io plasma torus would be centered on the magnetic equator of Jupiter. However, Jupiter is a fast rotating planet with a rotation period of 9.925 h. Consequently, the net effect of magnetic and centrifugal forces acting on the plasma causes the plasma to lie on the centrifugal equator (Cummings et al., 1980; Vasyliunas, 1983). For an idealized offset tilted dipolar (OTD) magnetic field, the centrifugal equator is a plane that lies two-thirds of the way from the rotational equator to the magnetic equator. Yet Jupiter's magnetic field possesses appreciable higher-order moments (Connerney et al., 2018). Their contributions to the magnetic field should distort the shape of the centrifugal equator, thereby displacing the Io plasma torus from its nominal location. Ground-based observations of the Io plasma torus have indeed shown that its shape is not perfectly toroidal and that it is not located precisely where the centrifugal equator would be for an idealized dipolar magnetic field (Herbert et al., 2008; Schneider & Trauger, 1995). The distribution of plasma perpendicular to the local centrifugal equator is characterized by a scale height. This is sensitive to the parallel ion temperature of plasma within the Io plasma torus (Khurana et al., 2004; Vasyliunas, 1983).

To understand the behavior of Jupiter's magnetosphere, the largest planetary object in the solar system, it is necessary to understand the behavior of the Io plasma torus, which is the source of most plasma in Jupiter's magnetosphere. In order to understand the behavior of the Io plasma torus, it is necessary to understand how plasma in the Io plasma torus is introduced into the torus, retained within the torus, and finally lost from the torus. Observations of fundamental properties of the torus (such as location, total electron content, and scale height) place valuable constraints on how the Io plasma torus behaves. For example, variations with System III longitude shed light on how Jupiter's magnetic field and associated phenomena affect the Io plasma torus. Conversely, variations with time and/or angle relative to Io shed light on how the flux of material away from Io affects the Io plasma torus.

Phipps et al. (2019) reported four observations of the Io plasma torus acquired at different System III longitudes on Juno Perijoves 1, 3, 6, and 8. All longitudes used here are System III longitudes discussed in Section 7. They found that peak total electron content and scale height vary appreciably between observations for the cold torus but not the torus beyond 5.5  $R_J$ . They could not determine whether these variations in the cold torus were caused by longitude, time, or other factors. They also found that the location of the torus differed from that predicted using an idealized dipolar magnetic field, noting as well that the cold torus was displaced from the torus beyond 5.5  $R_J$ . Phipps et al. (2020) showed that the locations of these two components of the torus were reproduced better by the Juno-era JRM09 model of the internal magnetic field of Jupiter than by the Voyager-era VIP4 model. Moreover, they also showed that these locations were reproduced best if the JRM09 internal field model was modified by the addition of the magnetic field induced by a simple current sheet model. This suggests that the location of the Io plasma torus is affected by magnetospheric conditions.

The aim of this manuscript is to further characterize spatial and temporal variations in fundamental properties of the Io plasma torus. This aim is achieved by the analysis and interpretation of observations from eight Juno Perijoves, four that were discussed previously by Phipps et al. (2018), Phipps et al. (2019), and Phipps et al. (2020) (PJ1, PJ3, PJ6, and PJ8) and four that are reported here for the first time (PJ10, 11, 14, and 15).

Section 2 describes Juno radio occultation observations of the Io plasma torus. Section 3 resolves a calibration problem that affected the analysis by Phipps et al. (2019) of data from PJ3, PJ6, and PJ8. Section 4 presents observations from PJ10, PJ11, PJ14, and PJ15. Section 5 compares the derived total electron content profiles to a model of the Io plasma torus. Section 6 describes how the location, peak total electron content, and scale height of the cold torus and the torus beyond 5.5  $R_J$  are determined by fitting the observed total electron content profiles. Section 7 discusses the results of Section 6. Section 7.1 assesses the dependence of fitted torus properties on longitude. Section 7.2 assesses the dependence of fitted torus properties on time. Section 7.3 assesses the dependence of fitted torus properties on Io phase angle. Section 7.4 presents the full set of total electron content profiles to highlight their similarities and differences. Section 7.5 uses observations from PJ8 and PJ15, which were acquired at the same longitude one year apart, to discriminate between effects of longitude and time on fitted torus properties. Section 8 states the conclusions of this article.

## 2. Overview of Juno Radio Occultation Observations of the Io Plasma Torus

The Juno spacecraft entered orbit around Jupiter on July 4, 2016. Its orbital period has remained constant at approximately 53 days. During each perijove, the Juno–Earth line of sight sweeps through one sector of the IPT. Some, but not all, Perijoves have a gravity science focus. During those Perijove, Juno points its high-gain antenna toward Earth and maintains a two-way coherent radio link with a ground station of the NASA Deep Space Network (DSN) at X-band and Ka-band frequencies. These X-band and Ka-band radio signals pass through the Io plasma torus, which affects their observed differential Doppler shift. A time series of the total electron content along the Juno–Earth line of sight can be determined from such observations. As the path of the Juno–Earth line of sight through the IPT changes with time during each perijove, this provides information on the spatial distribution of plasma in the Io plasma torus.

As explained in detail in Phipps et al. (2018) and Phipps et al. (2019), the observed differential Doppler shift is integrated with respect to time to yield an initial time series of the total electron content (TEC) along the Juno–Earth line of sight. Phipps et al. (2018) and Phipps et al. (2019) use a 10 s integration time. This article also uses a 10 s integration time for analysis of the IPT TEC. Before integration, the Doppler shift is corrected for the effects of Earth's troposphere, spacecraft spin, and ground station delays. The TEC contains several contributions from sources other than the Io plasma torus, such as Earth's ionosphere and the solar wind, which should be removed from the initial time series of TEC. First, contributions from Earth's ionosphere are subtracted from the initial time series of TEC to obtain the intermediate time series of TEC. This uses the line of sight total electron content of Earth's ionosphere, which is provided by a routine DSN data product estimated using GPS dual-frequency measurements (Buccino, 2016). Second, contributions from changes in the solar wind are subtracted from the intermediate time series of TEC to obtain the final time series of TEC. The intermediate time series of TEC still contains a contribution from changes in the TEC in the solar wind along the Juno–Earth line of sight. This is not directly measurable. Instead, a high-order polynomial function of time is fitted to the intermediate TEC values at times outside the interval of the Io plasma torus occultation. This baseline function is subtracted from the intermediate time series of TEC to obtain the final time series of TEC. Note that the steady state value of the solar wind TEC does not affect the observations.

The final time series of TEC is expressed as a one-dimensional function of position, where the relevant position coordinate for each Earth received time is a distance above the nominal plane of the centrifugal equator. Specifically, the distance above the nominal plane of the centrifugal equator of the point on that raypath whose projected distance from Jupiter in the nominal plane of the centrifugal equator is  $5.89 R_J$ , the orbital distance of Io. Values of the peak total electron content, the offset of the location of peak total electron content from the centrifugal equator, and the scale height are found for two components of the torus by fitting a pair of Gaussian functions of position to the final TEC values. The two fitted components of the torus are the cold torus and the torus beyond  $5.5 R_J$ , where the latter includes contributions from the warm torus and the ribbon. The Juno observations are not able to discriminate between the warm torus and ribbon, which have similar scale heights.

As of February 17, 2020, raw gravity science data from Perijoves PJ1, PJ3, PJ6, PJ8, PJ10, PJ11, PJ13, PJ14, PJ15, PJ17, and PJ18 have been generated, validated, and archived on the NASA Planetary Data System (PDS). Relevant gravity science data were not acquired on PJ2 (safe mode), PJ4, PJ5, PJ7, PJ9, PJ12, PJ16, PJ19, and PJ20 (high-gain antenna not Earth-pointed due to conflict with microwave radiometer observations, off-point observation mode (PJ12), or solar conjunction (PJ9)). Gravity science data from PJ1, PJ3, PJ6, and PJ8 were analyzed and reported by Phipps et al. (2018) and Phipps et al. (2019). Here, we report the processing and initial analysis of gravity science data from PJ10, PJ11, PJ14, and PJ15. Preliminary processing of gravity science data from PJ13 has been conducted. At the time of writing, results from PJ13 are unexpectedly complex. They await further analysis and are not discussed here.

## 3. Re-calibration of Previously Reported Results From PJ3, PJ6, and PJ8

The frequency observables are calibrated for instrumental effects such as spacecraft spin phase wrapping, Earth troposphere, and ground station delay similarly to Durante et al. (2020). The most pronounced instrumental effect is the ground station delay for both the uplink and downlink. Phipps et al. (2019) applied an ad hoc correction to data from PJ3, PJ6, and PJ8 to address what they inferred to be an instru-

mental bias of some kind. In response to this apparent bias, ground tests were conducted at DSS-25, the 34-m DSN antenna in Goldstone, California that conducted these observations. DSS-25 is currently the only DSN antenna capable of providing the Ka-band uplink used in nominal Juno gravity science observations. Previously, it was assumed the uplink delay and downlink delay were identical (77 microseconds each way). Accurate testing showed that the Ka-band uplink path contains an additional 24 microsecond delay when compared with the X-band uplink path (Buccino et al., 2019). Without accounting for the additional delay on the Ka-band uplink path, a bias is introduced in the measurement of the charged particle contents along the radio propagation path (Phipps et al., 2019). This work now fully accounts for this instrumental effect.

The re-calibrated data do not display the problems described by Phipps et al. (2019) and do not require any ad hoc correction. We used the re-calibrated data to re-derive total electron content profiles and associated fit parameters. Results are very similar to those of Phipps et al. (2019), which demonstrates that the ad hoc correction developed by Phipps et al. (2019) was reasonable. This issue did not affect PJ1, which used a different method for acquiring gravity science data (Phipps et al., 2018). Revised fit parameters for PJ3, PJ6, and PJ8 are listed in Section 6. For completeness, Section 6 also lists the fit parameters for PJ1, which are unchanged from Phipps et al. (2018).

#### 4. Data

The methods summarized in Section 2 and detailed in Phipps et al. (2019) were used to process gravity science data from PJ10, PJ11, PJ14, and PJ15, to generate total electron content profiles of the Io plasma torus, and to determine best-fit parameters for a model of the density distribution in the Io plasma torus.

Figures in Appendix A show the basic geometry of the Io plasma torus occultations on each of these Perijoves. Equivalent figures are shown in Figure 1 of Phipps et al. (2018) for PJ1 and Appendix A of Phipps et al. (2019) for PJ3, PJ6, and PJ8.

Figure 1 shows the differential Doppler shifts for PJ10, PJ11, PJ14, and PJ15. Equivalent figures are shown in Figure 2 of Phipps et al. (2018) for PJ1 and Figure 1 of Phipps et al. (2019) for PJ3, PJ6, and PJ8.

Phipps et al. (2019) states “to determine the X- and Ka-band frequency residuals, the X- and Ka-band Doppler observables ( $f_{obs}$ ) are combined to remove the effects of plasma noise (e.g., Mariotti & Tortora, 2013), and adjustments are applied for Earth’s ionosphere from GPS and troposphere either analytical models or water vapor radiometer measurement (when available). The spacecraft trajectory and Jupiter gravity field are then estimated using the calibrated Doppler observables, which are then used to compute the expected frequency ( $f_{comp}$ ).” A residual ( $\delta f$ ) is then computed for X- and Ka-band frequencies using the following equation (Phipps et al., 2019):

$$\delta f = f_{obs} - f_{comp} \quad (1)$$

These frequency residuals are related to the rate of change of the column electron content by (Parisi et al., 2018; Phipps et al., 2019):

$$\Delta f = \delta f_{R,X} - \delta f_{R,Ka} \left( \frac{f_{D,X}}{f_{D,Ka}} \right) = \frac{e^2}{8\pi^2 m_e \epsilon_0 c f_{T,X}} \left( \left( M_{X,X}^2 + 1 \right) - \left( \frac{f_{D,X}}{f_{D,Ka}} \right)^2 \left( M_{Ka,Ka}^2 + 1 \right) \right) \frac{d}{dt} \int N dl \quad (2)$$

The first equality defines  $\Delta f$ , which is called the differential Doppler shift. Here,  $\Delta f$  is the difference in frequency residuals, subscripts  $R$  and  $T$  refer to received and transmitted, respectively, subscript  $X$  refers to X-band, subscript  $Ka$  refers to Ka-band,  $c$  is the speed of light,  $t$  is time,  $l$  is distance along one leg of the two-way raypath,  $-e$  is the electric charge carried by the electron,  $m_e$  is the electron mass,  $\epsilon_0$  is the permittivity of free space, and  $N$  is the electron density. Note that the integral is performed over one leg of the two-way raypath only, not both legs. It is assumed that the plasma contents along the uplink and downlink ray paths are identical (Phipps et al., 2019). This is a good assumption if there is a short amount of time between when

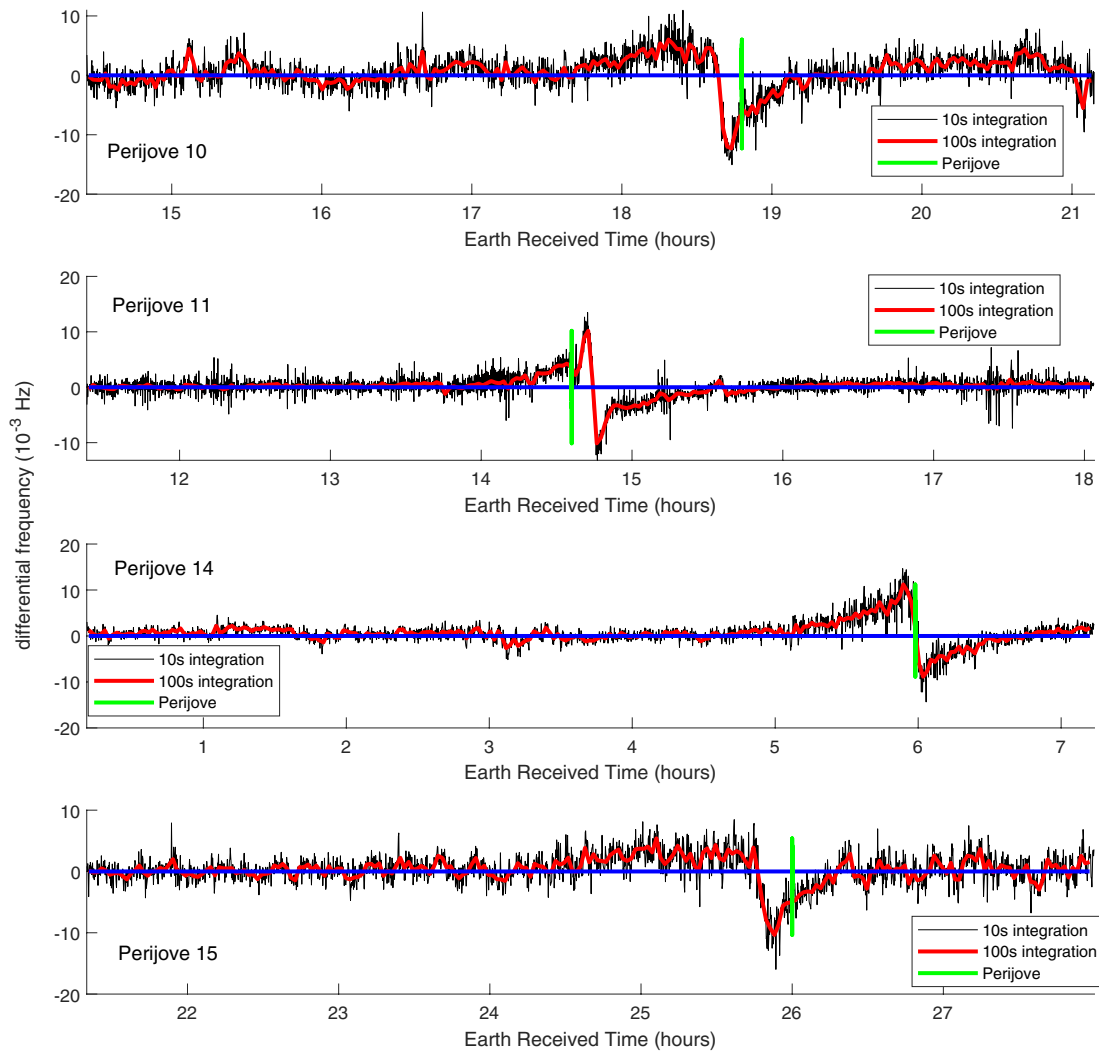


**Figure 1.** Time series of the observed differential Doppler shift between X-band and Ka-band frequencies for PJ10, PJ11, PJ14, and PJ15 (top to bottom). The black line shows observations at 10 s integration. The red line shows observations at 100 s integration. The vertical green line represents the time of perijove. The blue horizontal line indicates zero.

the uplink and downlink rays pass through the Io plasma torus. The individual frequency residuals are  $\delta f_{R,X}$  and  $\delta f_{R,Ka}$ . The ratio  $\frac{f_{D,X}}{f_{D,Ka}}$  is the ratio of the downlinked X-band frequency to the downlinked Ka-band frequency, equal to  $\frac{880}{3360}$  (Asmar et al., 2017).  $M_{X,X}$  is the spacecraft turnaround ratio for X-band uplink to X-band downlink,  $\frac{880}{749}$ , and  $M_{Ka,Ka}$  is the turnaround ratio for Ka-band uplink to Ka-band downlink,  $\frac{3360}{3599}$  (Asmar et al., 2017).

Figure 2 shows the initial, intermediate, and final time series of TEC values for PJ10, PJ11, PJ14, and PJ15. Equivalent figures are shown in Figure 3 of Phipps et al. (2018) for PJ1 and Figures 6–8 of Phipps et al. (2019) for PJ3, PJ6, and PJ8. As in Phipps et al. (2019), we fit a polynomial function to the time series of intermediate total electron content values outside the period in which the Io plasma torus is sampled, then delete that fitted baseline from the time series of intermediate total electron content values to obtain the time series of final total electron content values. The time ranges used for each perijove are listed in Table 1. Baselines for all Perijoves were fitted in the method of Phipps et al. (2019), although we use a fifth order polynomial rather than the ninth order polynomial of Phipps



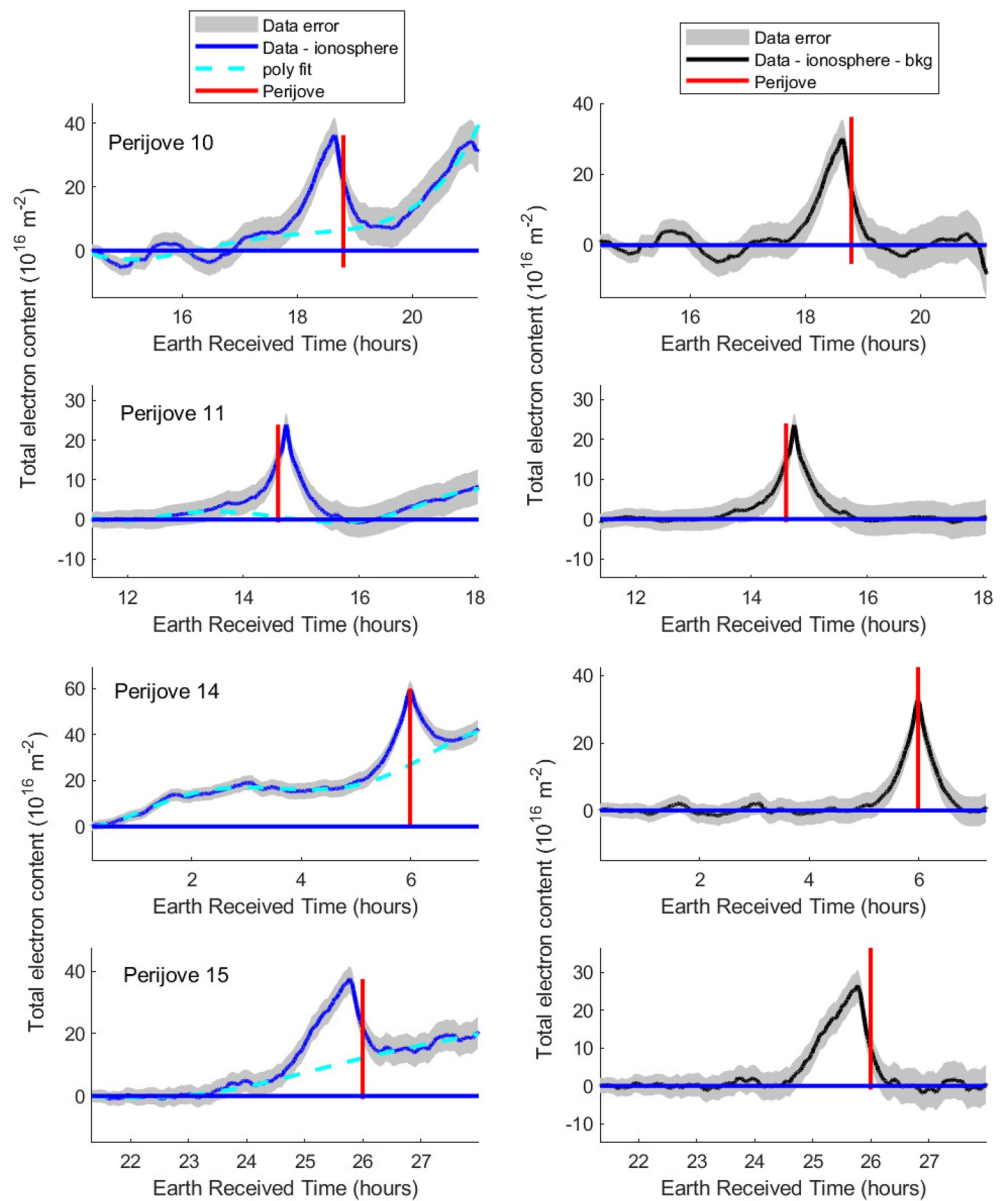


**Figure 2.** (left column) The blue curve shows the intermediate time series of TEC values (i.e., after correction for Earth's ionosphere). The cyan dashed line shows the polynomial background fit. The final time series of TEC values is generated by subtracting the polynomial background fit from the intermediate time series of TEC values (right column) The black curve shows the final time series of TEC values. (both columns) The gray shaded region shows the uncertainty on the TEC values, the red vertical line represents the time of perijove, and the blue horizontal line indicates the location of zero. From top to bottom, rows show data from PJ10, PJ11, PJ14, and PJ15. TEC, total electron content.

et al. (2019). The fifth order polynomials gave adequate results without overfitting the variations in the baseline. The only modification to the established correction method is on PJ10, where the baseline trend was unusually disturbed. An additional time period was excluded from this baseline fit, as defined in Table 1.

Final total electron content values are consistent with zero at times when the observations are outside the expected domain of the Io plasma torus.

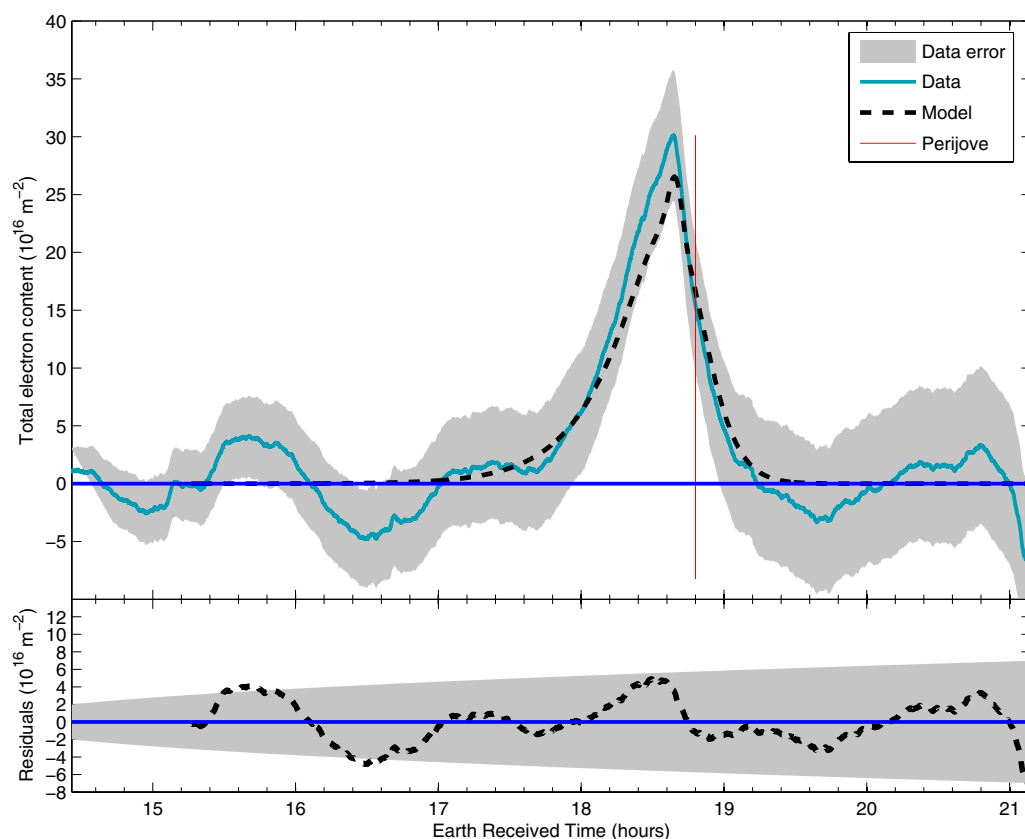


**Figure 3.** (top panel) The blue-green line shows the final time series of TEC values for PJ10. The black dashed line shows TEC values predicted by Model B of Phipps et al. (2018) (bottom panel) The black dashed line shows residuals between data and model. (both panels) The gray shaded region shows the uncertainty on the TEC values, the red vertical line represents the time of perijove, and the blue horizontal line indicates the location of zero. TEC, total electron content.

## 5. Data-Model Comparison

Here, we compare the observed TEC profiles to predictions from Model B of Phipps et al. (2018). Observed and predicted peak TEC values and times are listed in Table 2.

### 5.1. Perijove 10

Perijove 10 occurred on December 16, 2017. The model comparison is shown in Figure 3. The observed peak TEC value is 3.2 Total Electron Content Units (TECU) (12%) greater than predicted, where 1 TECU equals  $10^{16}$  electrons  $\text{m}^{-2}$ . The observed time of peak TEC is similar to the predicted time.

### 5.2. Perijove 11

Perijove 11 occurred on February 7, 2018. The model comparison is shown in Figure 4. The observed peak TEC value is 3.6 TECU (13.3%) less than the predicted. The observed time of peak TEC occurs 0.02 h earlier than predicted.

### 5.3. Perijove 14

Perijove 14 occurred on July 16, 2018. The model comparison is shown in Figure 5. The observed peak TEC value is 5.4 TECU (19.9%) greater than predicted. The observed time of peak TEC is 0.01 h earlier than predicted.



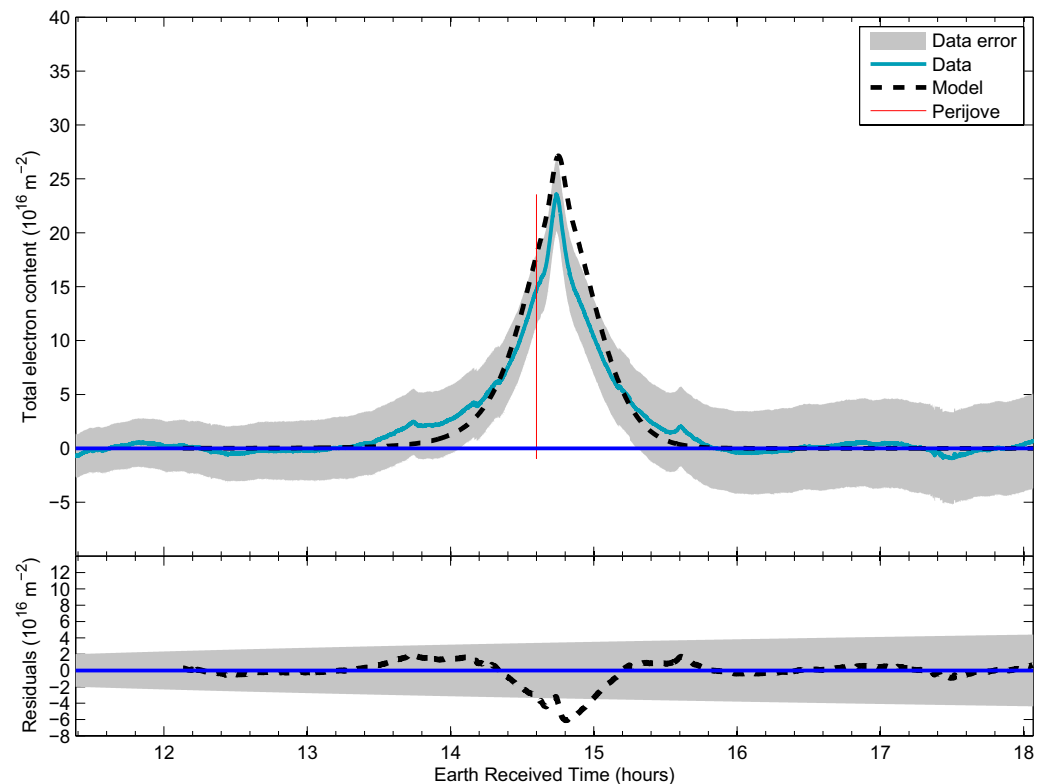


**Figure 4.** As Figure 3, but for PJ11.

#### 5.4. Perijove 15

Perijove 15 occurred on September 7, 2018. The model comparison is shown in Figure 6. The observed peak TEC value is only 0.1 TECU (2.6%) greater than predicted. The observed time of peak TEC is 0.02 h earlier than predicted.

#### 5.5. Initial Synthesis

Several findings arise from inspection of Figures 3–6. First, observed and predicted times of peak total electron content are more similar than was the case for PJ1–PJ8 (Phipps et al., 2019). Second, observed and predicted values of peak total electron content differ by roughly 10%. Third, once these differences in peak total electron content are taken into consideration, the relative shapes of the predicted and observed time series of total electron content are more similar than was the case for PJ1–PJ8 (Phipps et al., 2019). Displacement in time between the observed and predicted TEC profiles would suggest displacement of the torus from the model’s centrifugal equator, as discussed by Phipps et al. (2018) and Phipps et al. (2019) for PJ1, PJ3, PJ6, and PJ8. Therefore, the first and third findings suggest that, in these observations, the location of the Io plasma torus is relatively close to the expected centrifugal equator.

### 6. Fit of Two Gaussian Functions to TEC Data

In order to better interpret the initial impressions reported in Section 5.5, we fit the observed TEC profiles and consider the resultant fit parameters. Instead of fitting the observed TEC as a function of time, we fit TEC as a function of  $z$ . For each Earth received time, and hence each line of sight,  $z$  is defined as the  $z$ -coordinate of the point along the Juno–Earth line of sight whose value of  $\sqrt{(x^2 + y^2)}$  equals  $5.89 R_J$ , the orbital

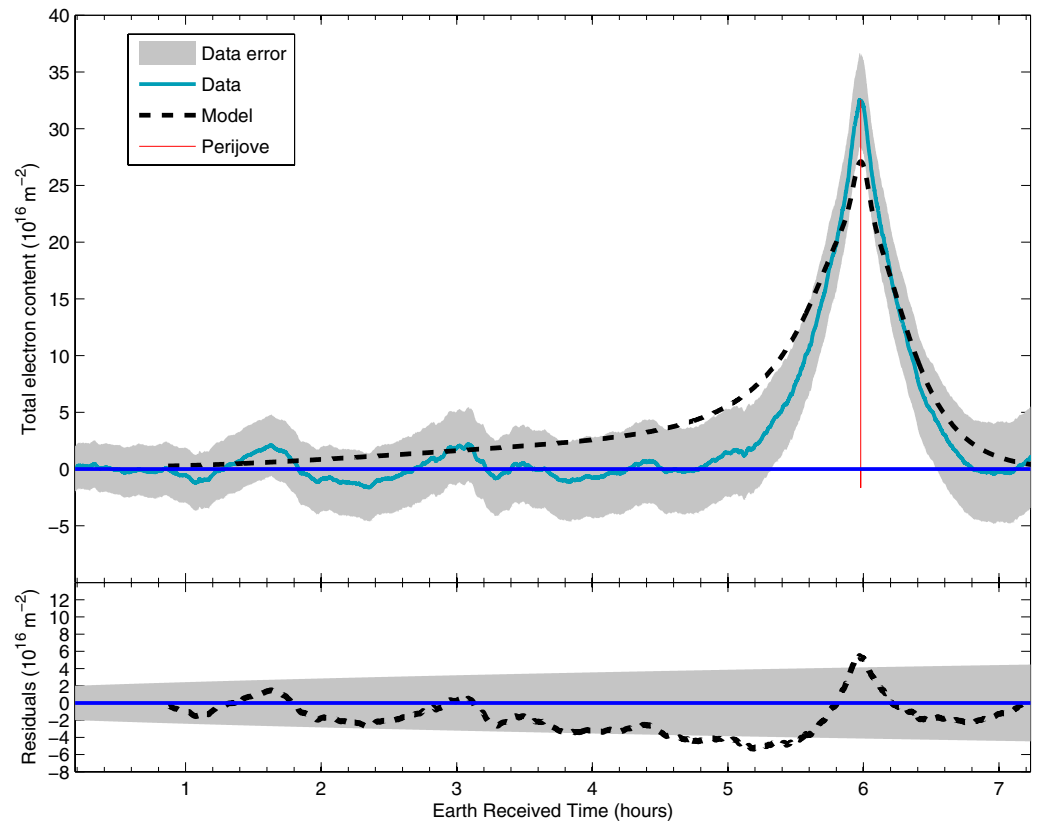


**Figure 5.** As Figure 3, but for PJ14.

distance of Io. Here,  $x$ ,  $y$ , and  $z$  are expressed in the centrifugal coordinate system introduced in Section 2 of Phipps et al. (2018). This position coordinate can be considered as the distance above the centrifugal equator at which the line-of-sight encounters the torus.

The data are now fit using the two-Gaussian function from Phipps et al. (2018) and Phipps et al. (2019). This fit function is

$$TEC(z) = a_1 e^{-(z-b_1)^2/c_1^2} + a_2 e^{-(z-b_2)^2/c_2^2}, \quad (3)$$

where  $z$  is the distance from the centrifugal equator,  $a_n$  is the peak TEC,  $b_n$  is the peak location offset, and  $c_n$  is the scale height. This function is used with PJ10, PJ11, PJ14, and PJ15 to derive the peak TEC, peak location offset, and scale height for both the cold torus (smaller scale height, subscript 1) and torus beyond  $5.5 R_J$  (larger scale height, subscript 2). The ribbon and warm torus are combined into “the torus beyond  $5.5 R_J$ ” as the data are not sufficient to constrain a third Gaussian term (Phipps et al., 2018; Phipps et al., 2019).

The resulting fit parameters for PJ10, PJ11, PJ14, and PJ15 are presented in Table 3. For each perijove, predicted, initial guess, and best-fit values of fit parameters are provided. Predicted fit parameters come from a fit to Model B of Phipps et al. (2018) using appropriate geometry for each occultation. Initial guess fit parameters come from fitting the data using the MatLab curve fitting routine. The best-fit values of fit parameters come from fitting the data using a Markov Chain Monte Carlo (MCMC) python routine that assumes a normal distribution for the parameters (Foreman-Mackey et al., 2013) and uses the stated initial guesses.  $10^5$  runs were conducted for each perijove; the resultant best-fit values and their uncertainties are reported in Table 3. Table 3 also lists the parameters for PJ1 and the updated parameters for PJ3, PJ6, and PJ8.

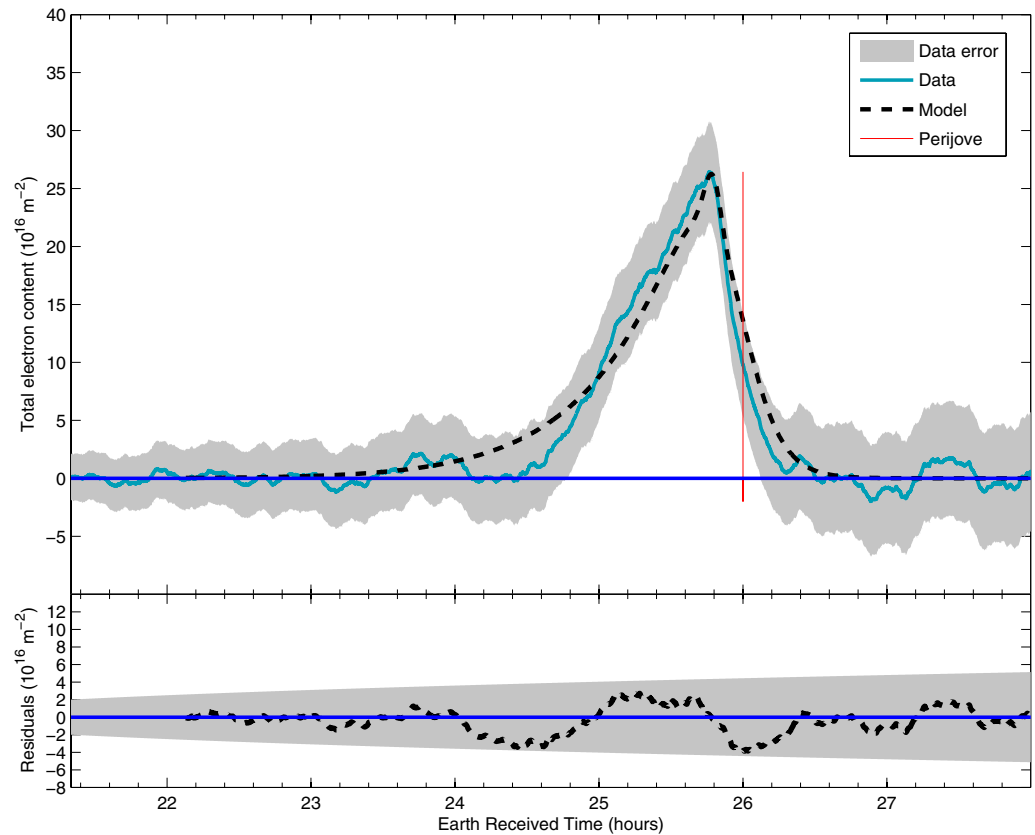


**Figure 6.** As Figure 3, but for PJ15.

### 6.1. Perijove 10

The fit to PJ10 data is shown in Figure 7. The values of the fit parameters are shown in Table 3. For the cold torus, the peak total electron content is  $98 \pm 20$  percent of the predicted value and the scale height is  $100 \pm 28$  percent of the predicted value. For the torus beyond  $5.5 R_J$ , the peak total electron content is  $117 \pm 7$  percent of the predicted value and the scale height is  $85 \pm 6$  percent of the predicted value. The reduced chi-square,  $\chi^2$ , for the fit was 0.0034. Since there is an unknown in the uncertainty in the background subtraction, we inflate our data uncertainty to account for any background. This was done by assuming an uncertainty of 2 TECU on the background polynomial fit and 2 TECU for the Earth's ionosphere. Then use error propagation, using subtraction method since the background and Earth's ionosphere TEC are subtracted from the total TEC, to combine the errors on the data, background, and Earth's ionosphere to determine the error on the final data (Phipps & Withers, 2017; Phipps et al., 2018) This leads to an overestimation of uncertainty and a  $\chi^2$  less than one. This is true for all observations.

Parameters  $b_1$  and  $b_2$  indicate offsets in the fitted peak total electron contents from the OTD nominal centrifugal equator. Both predicted offsets are nonzero, even though the model was defined to be symmetric about the centrifugal equator. Specifically, the peak offset values for the model are  $-0.069 R_J$  for  $b_1$  and  $0.089 R_J$  for  $b_2$  during PJ10.

As discussed in Phipps et al. (2018), these nonzero values are artifacts of the geometry between the Juno-Earth lines-of-sight and the Io plasma torus (e.g., Figures presented in Appendix A). The lines-of-sight are not parallel to the OTD nominal centrifugal equator. When the PJ10 line of sight passes through the OTD nominal centrifugal equator at  $\sqrt{x^2 + y^2} = 5.89 R_J$ , the expected distance of peak density in the torus beyond  $5.5 R_J$ , Juno is at  $\sqrt{x^2 + y^2} = 0.943 R_J$  and  $z = 0.669 R_J$ . Therefore, this line of sight is at an angle of  $7.70^\circ$  to the OTD nominal centrifugal equator. Consequently, the line of sight for which the model cold torus TEC is greatest passes through the OTD nominal centrifugal equator at a radial distance of  $5.38 R_J$ .

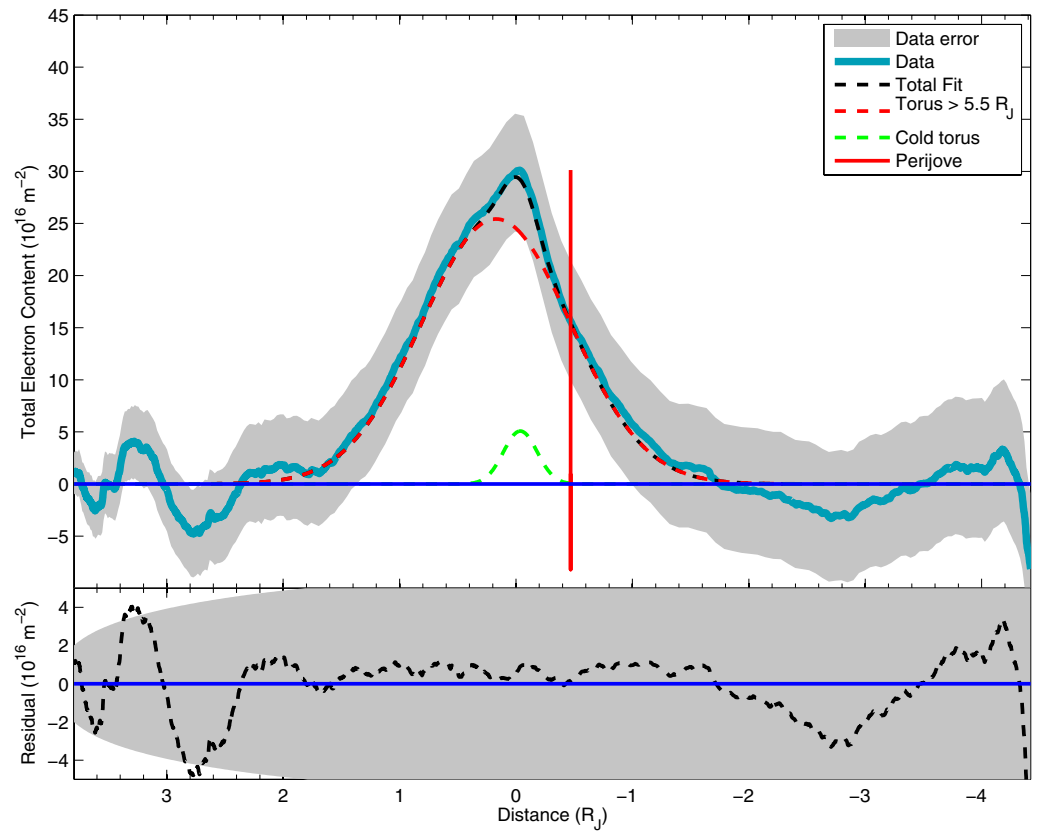


**Figure 7.** (top panel) Two Gaussian fit to final TEC values for PJ10. The blue-green line shows the data. The dashed black line is the fitted two Gaussian model, the red line shows the contribution of the torus beyond  $5.5 R_J$ , and the green dashed line shows the contribution of the cold torus. (bottom panel) The black dashed line shows residuals between data and the fitted model. (both panels) The gray shaded region shows the uncertainty on the TEC values, the red vertical line represents the time of perijove, and the blue horizontal line indicates the location of zero. TEC, total electron content.

Similarly, the line of sight for which the model “torus beyond  $5.5 R_J$ ” TEC is greatest passes through the OTD nominal centrifugal equator at a radial distance of  $6.55 R_J$ . As discussed below, these radial distances were used to infer the tilt of the torus.

Differences between predicted positions and best-fit positions (Table 3) indicate how observed torus regions are displaced from their expected locations.  $\Delta b_1$  is  $0.032 \pm 0.033 R_J$  for the cold torus and  $\Delta b_2$  is  $0.083 \pm 0.012 R_J$  for the torus beyond  $5.5 R_J$ . As discussed in Phipps et al. (2018), each offset can be related to the angular tilt of the observed plane of that torus region relative to the predicted plane in the OTD nominal centrifugal

equator. Specifically, the angular tilt  $\alpha_n = \arcsin\left(\frac{\Delta b_n}{R_n}\right)$ .  $R_n$  is the radial peak location of the cold torus and the torus beyond  $5.5 R_J$  ( $5.38$  and  $6.55 R_J$ , respectively, as discussed above).

In this representation, a positive  $\alpha_n$  corresponds to the observed plane of the torus being above the nominal centrifugal equator and a negative  $\alpha_n$  corresponds to the observed plane of the torus being below the nominal centrifugal equator. For PJ10, we used the values stated above to find tilt angles  $\alpha_n$  of  $0.340 \pm 0.351^\circ$  for the cold torus and  $0.727 \pm 0.105^\circ$  for the torus beyond  $5.5 R_J$ .

## 6.2. Perijove 11

The fit to PJ11 data is shown in Figure 8. The values of the fit parameters are shown in Table 3. For the cold torus, the peak total electron content is  $123 \pm 11$  percent of the predicted value and the scale height is  $81 \pm 6$  percent of the predicted value. For the torus beyond  $5.5 R_J$ , the peak total electron content is  $78 \pm 16$

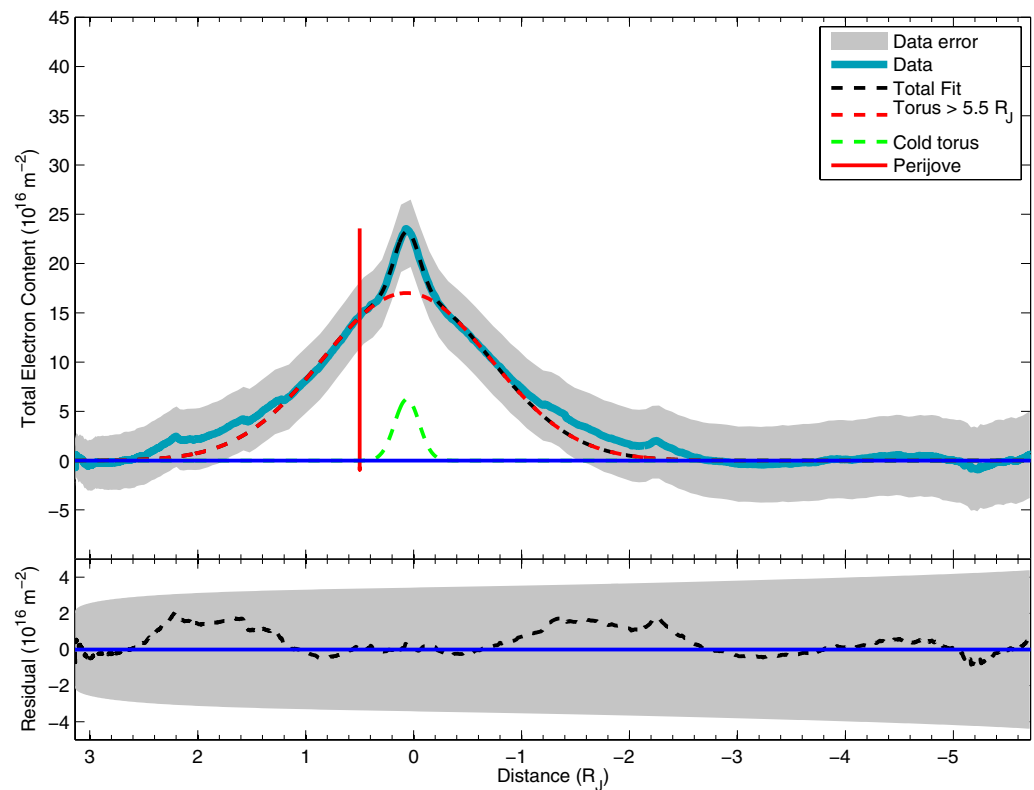


**Figure 8.** As Figure 7, but for PJ11.

percent of the predicted value and the scale height is  $103 \pm 18$  percent of the predicted value. The reduced chi-square,  $\chi^2$ , for the fit was 0.0063.

The peak offset values for the model are  $0.0269 R_J$  for  $b_1$  and  $0.0071 R_J$  for  $b_2$  during PJ11. When the PJ11 line of sight passes through the OTD nominal centrifugal equator at  $\sqrt{x^2 + y^2} = 5.89 R_J$ , the radial distance of the peak of the torus beyond  $5.5 R_J$ , Juno is at  $\sqrt{x^2 + y^2} = 1.20 R_J$  and  $z = -0.099 R_J$ . Therefore this line of sight is at an angle of  $-1.20^\circ$  to the OTD nominal centrifugal equator. Consequently, the line of sight for which the model cold torus TEC is greatest passes through the OTD nominal centrifugal equator at a radial distance of  $4.61 R_J$ . Similarly, the line of sight for which the model “torus beyond  $5.5 R_J$ ” is greatest passes through the OTD nominal centrifugal equator at a radial distance of  $5.55 R_J$ .

**Table 1**  
Time Periods Excluded From Baseline Fit for Perijoves 10, 11, 14, and 15

Perijove	Period of torus observation UTC	Additional exclusions UTC
Perijove 10	17:41–19:08	>21:09
Perijove 11	13:33–15:49	–
Perijove 14	04:58–06:51	–
Perijove 15	23:39–02:23	–

In all cases, time periods when the torus is sampled are excluded from the baseline fit. For PJ15, note that this period is from late on September 6, 2018 to early on September 7, 2018. In the case of PJ10 only, the complicated background demanded the exclusion of additional periods of data.

$\Delta b$  is  $0.035 \pm 0.006 R_J$  for the cold torus and  $\Delta b_2$  is  $0.058 \pm 0.049 R_J$  for the torus beyond  $5.5 R_J$ . Using these values, we find tilt angles  $\alpha_n$  of  $0.440 \pm 0.085^\circ$  for the cold torus and  $0.598 \pm 0.538^\circ$  for the torus beyond  $5.5 R_J$ .

### 6.3. Perijove 14

The fit to PJ14 data is shown in Figure 9. The values of the fit parameters are shown in Table 3. For the cold torus, the peak total electron content is  $137 \pm 17$  percent of the predicted value and the scale height is  $92 \pm 8$  percent of the predicted value. For the torus beyond  $5.5 R_J$ , the peak total electron content is  $114 \pm 10$  percent of the predicted value and the scale height is  $76 \pm 8$  percent of the predicted value. The reduced chi-square,  $\chi^2$ , for the fit was 0.0196.

**Table 2**

Observed and Predicted Time and Value of Maximum Total Electron Content for PJ10, PJ11, PJ14, and PJ15. Peak Time is Observed Time of Maximum Total Electron Content. Peak TEC is Observed Value of Maximum Total Electron Content. Model Time is Predicted Time of Maximum Total Electron Content in the Model B of Phipps et al. (2018). Model TEC is Predicted Value of Maximum Total Electron Content in the Model B of Phipps et al. (2018)

Perijove	Date	Peak time Hours	Peak TEC TECU	Model time hours	Model TEC TECU
Perijove 10	December 16, 2017	$18.65 \pm 0.07$	$29.8 \pm 2.6$	18.65	26.6
Perijove 11	February 7, 2018	$14.73 \pm 0.03$	$23.5 \pm 2.2$	14.75	27.1
Perijove 14	July 16, 2018	$5.97 \pm 0.04$	$32.5 \pm 2.3$	5.98	27.1
Perijove 15	September 7, 2018	$25.76 \pm 0.11$	$26.4 \pm 2.3$	25.78	26.3

Abbreviations: TEC, total electron content; TECU, total electron content unit.

**Table 3**

Parameters of two Gaussian fit to Observed TEC profiles. As discussed in the Text, Predicted Values are From a Fit to Model B of Phipps et al. (2018), Initial Guess Values are From a Preliminary Fit to Observations, and Best-Fit Values are From a Final Fit to Observations

Value	Peak TEC $a_1$ TECU	Cold torus Offset $b_1$ $R_J$	Scale height $c_1$ $R_J$	Peak TEC $a_2$ TECU	Torus $R > 5.5 R_J$ Offset $b_2$ $R_J$	$c_2$ $R_J$
Perijove 1	$8.18 \pm 1.80$	$-0.044 \pm 0.024$	$0.348 \pm 0.051$	$29.3 \pm 2.7$	$-0.246 \pm 0.056$	$1.18 \pm 0.13$
Perijove 3	$3.21 \pm 0.75$	$0.013 \pm 0.019$	$0.176 \pm 0.039$	$23.3 \pm 2.7$	$0.230 \pm 0.036$	$0.885 \pm 0.083$
Perijove 6	$8.27 \pm 0.81$	$0.025 \pm 0.008$	$0.172 \pm 0.014$	$22.2 \pm 2.9$	$-0.089 \pm 0.044$	$0.936 \pm 0.123$
Perijove 8	$12.2 \pm 1.6$	$-0.079 \pm 0.012$	$0.231 \pm 0.025$	$26.7 \pm 2.8$	$0.200 \pm 0.059$	$0.926 \pm 0.079$
Perijove 10						
Predicted	5.16	-0.069	0.206	21.7	0.089	1.06
Initial guess	4.98	-0.042	0.175	26.7	0.175	0.933
Best-fit	$5.08 \pm 1.03$	$-0.037 \pm 0.033$	$0.205 \pm 0.058$	$25.4 \pm 1.5$	$0.172 \pm 0.012$	$0.905 \pm 0.063$
Perijove 11						
Predicted	5.08	0.0269	0.200	22.0	0.0071	1.07
Initial guess	7.36	0.063	0.212	15.6	0.05	1.25
Best-fit	$6.23 \pm 0.55$	$0.062 \pm 0.006$	$0.162 \pm 0.011$	$17.1 \pm 3.5$	$0.065 \pm 0.049$	$1.10 \pm 0.19$
Perijove 14						
Predicted	5.36	-0.011	0.212	21.6	0.044	1.12
Initial guess	7.66	0.013	0.203	24.6	-0.031	0.862
Best-fit	$7.34 \pm 0.89$	$0.0039 \pm 0.0085$	$0.194 \pm 0.018$	$24.6 \pm 2.1$	$-0.0046 \pm 0.0260$	$0.855 \pm 0.085$
Perijove 15						
Predicted	5.15	-0.074	0.206	21.6	0.113	1.06
Initial guess	5.59	-0.073	0.231	22.7	0.241	0.923
Best-fit	$6.31 \pm 1.52$	$-0.077 \pm 0.026$	$0.252 \pm 0.052$	$22.4 \pm 2.9$	$0.259 \pm 0.069$	$0.998 \pm 0.132$

Abbreviations: TEC, total electron content; TECU, total electron content unit.



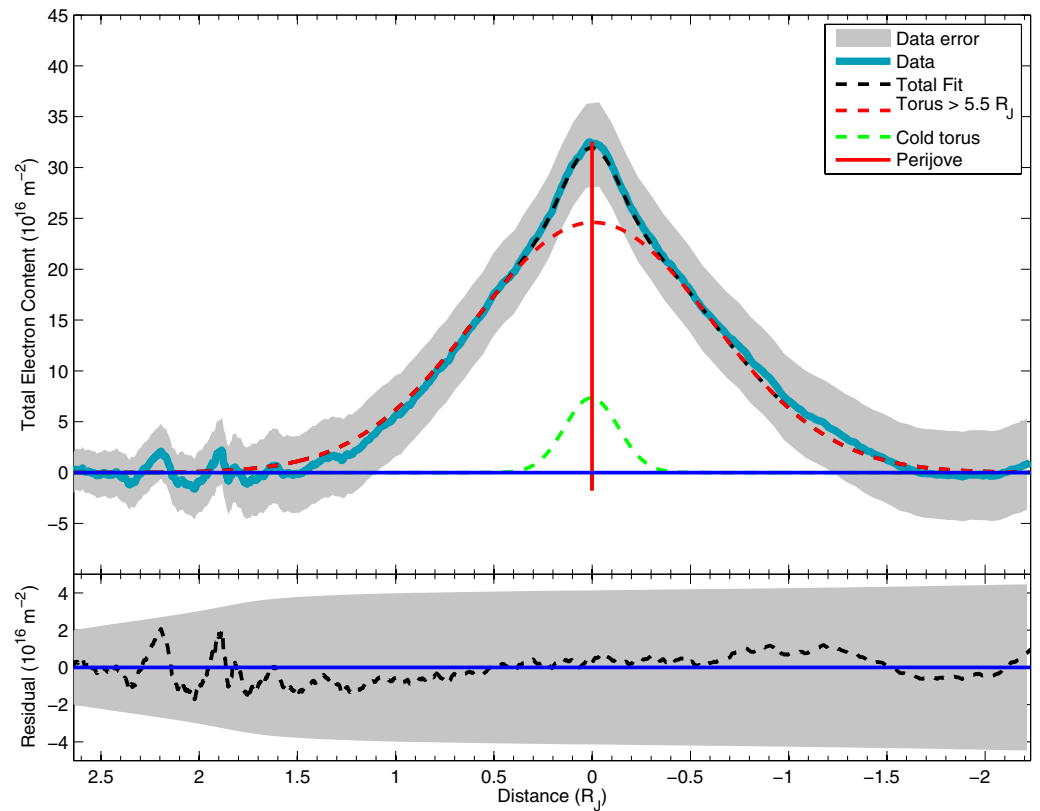


**Figure 9.** As Figure 7, but for PJ14.

The peak offset values for the model are  $-0.011 R_J$  for  $b_1$  and  $0.044 R_J$  for  $b_2$  during PJ14. When the PJ14 line of sight passes through the OTD nominal centrifugal equator at  $\sqrt{x^2 + y^2} = 5.89 R_J$ , the radial distance of the peak of the torus beyond  $5.5 R_J$ , Juno is at  $\sqrt{x^2 + y^2} = 0.912 R_J$  and  $z = 0.203 R_J$ . Therefore this line of sight is at an angle of  $2.34^\circ$  to the OTD nominal centrifugal equator. Consequently, the line of sight for which the model cold torus TEC is greatest passes through the OTD nominal centrifugal equator at a radial distance of  $5.61 R_J$ . Similarly, the line of sight for which the model “torus beyond  $5.5 R_J$ ” is greatest passes through the OTD nominal centrifugal equator at a radial distance of  $6.97 R_J$ .

$\Delta b$  is  $0.015 \pm 0.009 R_J$  for the cold torus and  $\Delta b_2$  is  $-0.049 \pm 0.026 R_J$  for the torus beyond  $5.5 R_J$ . Using these values, we find tilt angles  $\alpha_n$  of  $0.155 \pm 0.087^\circ$  for the cold torus and  $-0.398 \pm 0.213^\circ$  for the torus beyond  $5.5 R_J$ .

#### 6.4. Perijove 15

The fit to PJ15 data is shown in Figure 10. The values of the fit parameters are shown in Table 3. For the cold torus, the peak total electron content is  $123 \pm 30$  percent of the predicted value and the scale height is  $122 \pm 25$  percent of the predicted value. For the torus beyond  $5.5 R_J$ , the peak total electron content is  $104 \pm 13$  percent of the predicted value and the scale height is  $94 \pm 12$  percent of the predicted value. The reduced chi-square,  $\chi^2$ , for the fit was 0.024.

The peak offset values for the model are  $-0.074 R_J$  for  $b_1$  and  $0.113 R_J$  for  $b_2$  during PJ15. When the PJ15 line of sight passes through the OTD nominal centrifugal equator at  $\sqrt{x^2 + y^2} = 5.89 R_J$ , the radial distance of the peak of the torus beyond  $5.5 R_J$ , Juno is at  $\sqrt{x^2 + y^2} = 0.765 R_J$  and  $z = 0.849 R_J$ . Therefore this line of sight is at an angle of  $9.41^\circ$  to the OTD nominal centrifugal equator. Consequently, the line of sight for which the model cold torus TEC is greatest passes through the OTD nominal centrifugal equator at a radial

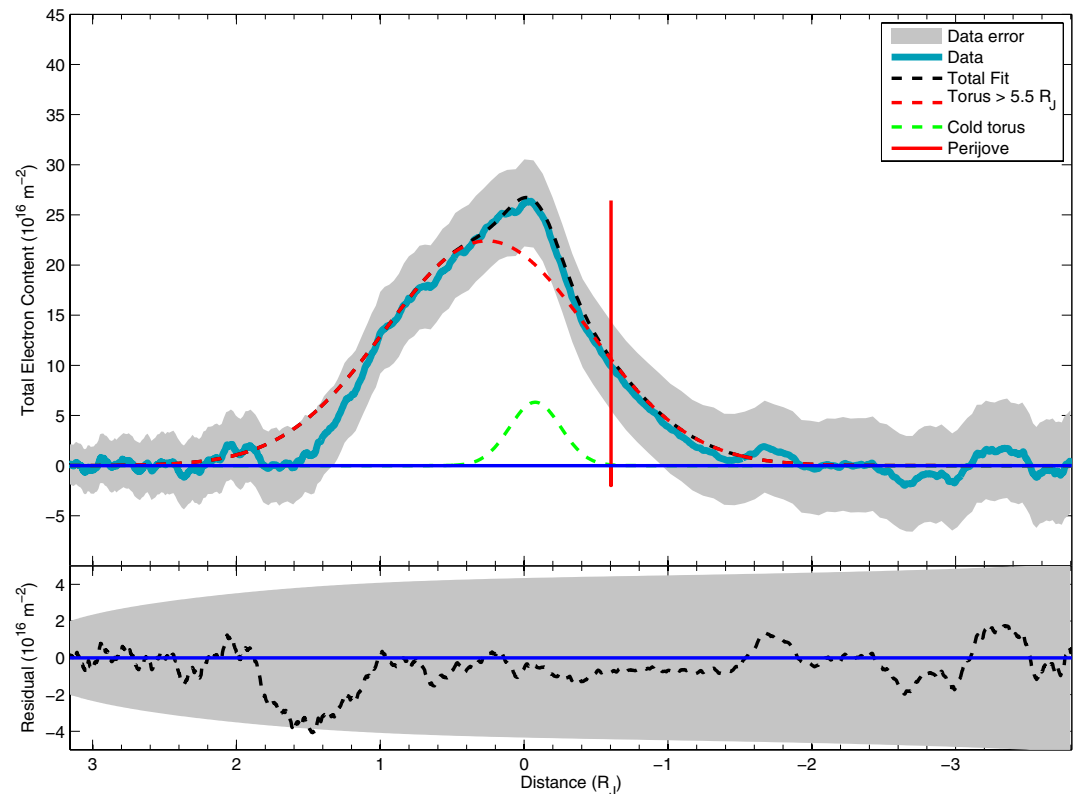


**Figure 10.** As Figure 7, but for PJ15.

distance of  $5.44 R_J$ . Similarly, the line of sight for which the model “torus beyond  $5.5 R_J$ ” is greatest passes through the OTD nominal centrifugal equator at a radial distance of  $6.57 R_J$ .

$\Delta b$  is  $-0.003 \pm 0.026 R_J$  for the cold torus and  $\Delta b_2$  is  $0.146 \pm 0.069 R_J$  for the torus beyond  $5.5 R_J$ . Using these values, we find tilt angles  $\alpha_n$  of  $-0.031 \pm 0.274^\circ$  for the cold torus and  $1.27 \pm 0.60^\circ$  for the torus beyond  $5.5 R_J$ .

## 7. Discussion

The System III longitudes sampled by the observations on PJ10, PJ11, PJ14, and PJ15 are shown in Table 4. The standard “System III” coordinate system is Jupiter’s rotational reference frame and is a left handed reference frame (Bagenal, Adriani, et al., 2017). The Z-axis is defined by the spin axis of Jupiter, the X-axis is defined by  $0^\circ$  latitude on System III longitude  $0^\circ$ . The Y-axis completes the orthogonal basis  $Y = X \times Z$ . As shown in Figure 11, the observations on PJ10, PJ11, and PJ14 fill in gaps in the System III longitude coverage provided by observations on earlier Perijoves (Phipps et al., 2018; Phipps et al., 2019). The System III longitude coverage of Juno radio occultation observations of the Io plasma torus is now reasonably complete. If the density distribution in the Io plasma torus is constant in time, but dependent on System III longitude in a smoothly varying manner, then the available observations are sufficient to characterize this dependence on System III longitude. Furthermore, the observation on PJ15 at  $8^\circ$  System III longitude was very close to the earlier observation on PJ8 at  $10^\circ$  System III longitude. These two observations permit a direct test for time variations.

### 7.1. Variations with System III Longitude

#### 7.1.1. Angular Tilt

Ground-based observations have shown the Io plasma torus emissions do not appear to be in a planar geometry Schneider and Trauger (1995); Herbert et al. (2008); Schmidt et al. (2018). Phipps et al. (2020) showed, using magnetic field models including higher order moments and the current sheet, that the centrifugal equator does not lie in a plane as in the offset tilted dipole magnetic field geometry. The dependence

**Table 4**

*Date, Time, and System III Longitude for Juno Radio Occultations on PJ10–PJ15. The Start and End Times Correspond to When the Juno–Earth Lines of Sight Encounter Local Density of More Than  $250 \text{ cm}^{-3}$  in the Io Plasma Torus. Values from Phipps et al. (2019) for PJ1, PJ3, PJ6, and PJ8 are Added for Reference*

Perijove	Date	Torus start Time UTC	Torus peak Time UTC	Torus end Time degrees	Torus start $\lambda_{\text{III}}$ Degrees	Torus peak $\lambda_{\text{III}}$ Degrees	Torus end $\lambda_{\text{III}}$ degrees	Io phase Angle degrees
Perijove 1	August 27, 2016					184		198
Perijove 3	December 11, 2016					60		214
Perijove 6	May 19, 2017					213		346
Perijove 8	September 2, 2017					10		96
Perijove 10	December 16, 2017	17:38	18:38	19:38	303	329	8	179
Perijove 11	February 7, 2018	13:45	14:45	15:45	213	243	285	234
Perijove 14	July 16, 2018	4:59	5:59	6:59	83	109	151	346
Perijove 15	September 7, 2018	0:45	1:45	2:45	342	8	46	40

of angular tilts on System III longitude are shown in Figure 11. All cold torus angular offsets are within 1 standard deviation of the sinusoidal variation observed by Schneider and Trauger (1995).

As expected from Section 5.5, angular tilts for PJ10, PJ11, PJ14, and PJ15 are relatively small. The tilt angles define the relative position of the total electron content to the “nominal” centrifugal equator from the dipolar approximation. Therefore, a negative angle means the data lies below the “nominal” centrifugal equator and a positive angle means the data lie above the “nominal” centrifugal equator. A value of zero means the data is on “nominal” centrifugal equator.

In general, the magnitude of the angular offset of the torus beyond  $5.5 R_J$  is larger than the magnitude of the angular offset of the cold torus, and the signs of the angular offsets of the two torus components are the same. Perijove 11 is an exception in that the angular offset of its torus beyond  $5.5 R_J$  is closer to zero than the angular offset of its cold torus. Phipps et al. (2018) reported absolute values of tilts for PJ1 without emphasizing direction. Their inferred tilt values were negative (e.g.,  $-0.9^\circ \pm 0.1^\circ$  for the cold torus and  $-1.7^\circ \pm 0.2^\circ$  for the torus beyond  $5.5 R_J$ ).

The System III longitudes sampled by PJ8 and PJ15 are very similar, 10 and  $8^\circ$  respectively. The angular offsets of their torus components are very similar, despite the 12 months interval between the two observations. The angular offsets of the cold torus were  $0.035^\circ \pm 0.129^\circ$  and  $-0.031^\circ \pm 0.274^\circ$  for PJ8 and PJ15, respectively. The angular offsets of the torus beyond  $5.5 R_J$  were  $0.875^\circ \pm 0.530^\circ$  and  $1.27^\circ \pm 0.60^\circ$  for PJ8 and PJ15, respectively. The similarities between the angular offsets found for PJ8 and PJ15 suggest that the shapes of the Io plasma torus, the centrifugal equator, and the magnetic equator are constant with time. Further observations of the Io plasma torus by Juno radio occultations will test whether this holds as repeat observations occur at other System III longitudes.

Figure 12 compares observed locations of the Io plasma torus to predicted locations of the centrifugal equator. The top panel shows predicted centrifugal equator found from the JRM09 model (Connerney et al., 2018) of the internal magnetic field as described in more detail by Phipps et al. (2020). In the bottom panel the predicted centrifugal equator was found from the combination of the JRM09 model of the internal magnetic field and a model of the magnetic field generated by the magnetospheric current sheet (Connerney et al., 1981), as described in more detail by Phipps et al. (2020).

The results for PJ1–PJ15 (8 Perijoves) in Figure 12 are consistent with the earlier results of Phipps et al. (2020) for PJ1–PJ8 (4 Perijoves). Using the JRM09 model only, the location of the cold torus is predicted relatively well, but the location of the torus beyond  $5.5 R_J$  is not. With the addition of a nominal current sheet model, the predicted location of the cold torus worsens, but the predicted location of the torus beyond  $5.5 R_J$  improves. Overall, it appears that magnetic field conditions around  $5.3 R_J$  (representative radial distance of the cold torus) are adequately represented by an internal field model without the need for appreciable contributions from the external field generated by the magnetospheric current sheet. Yet, magnetic field conditions around  $5.9 R_J$  (representative radial distance of the torus beyond  $5.5 R_J$ )

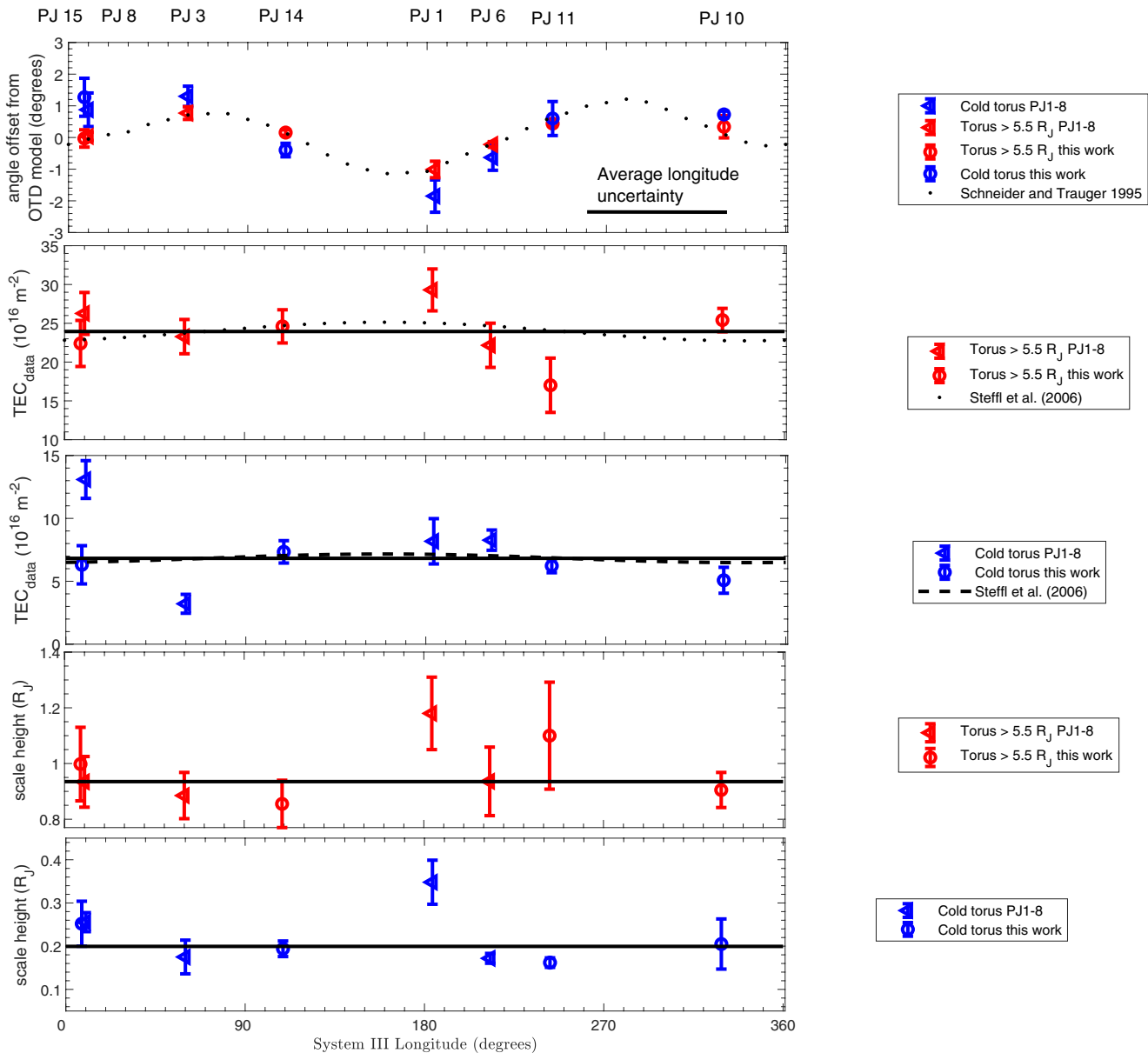


**Figure 11.** (a) Dependence on System III longitude of angular offsets in locations of torus regions from nominal centrifugal equator. These angular offsets are between the observed locations of these regions and the offset tilted dipole nominal centrifugal equator used in this work. The dotted line shows the angular offset of the ribbon relative to the offset tilted dipole nominal centrifugal equator based on ground-based optical observations (Schneider & Trauger, 1995; Phipps et al., 2019). (b) Dependence on System III longitude of fitted peak total electron content of the torus beyond  $5.5 R_J$ . Horizontal lines show the median value of the Juno observations. The dotted line shows a prediction based upon Cassini ultraviolet spectrometer observations (Steffl et al., 2006; Phipps et al., 2019). (c) As panel (b), but for the cold torus. The dashed line shows a prediction based upon Cassini ultraviolet spectrometer observations (Steffl et al., 2006; Phipps et al., 2019). (d) Dependence on System III longitude of fitted scale height of the torus beyond  $5.5 R_J$ . Horizontal lines show the median values of the Juno observations. (e) As panel (d), but for the cold torus. (all) Blue and red symbols show Juno radio occultation results for the cold torus and torus beyond  $5.5 R_J$ , respectively. Circles and triangles represent this work and the work of Phipps et al. (2019), respectively. The Perijoves are labeled at the top of the figure in plot order from left to right.

require contributions from both an internal field and an external field. This effect is responsible for the differences seen between the locations of the cold torus and the torus beyond  $5.5 R_J$ . As radial distance increases, the centrifugal equator tends to move toward the magnetic equator predicted by an internal field model.

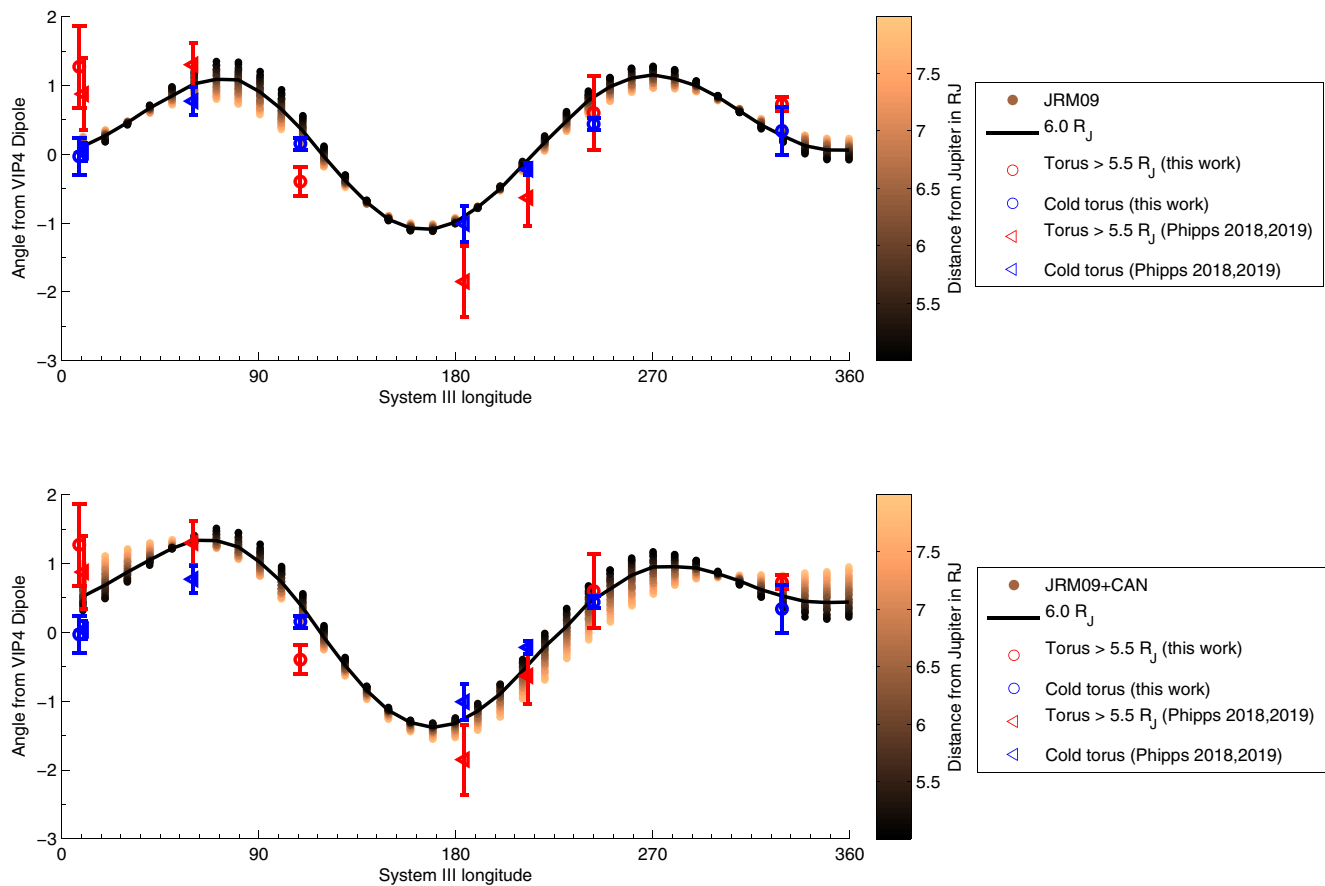


**Figure 12.** (all) Dependence on System III longitude of angular offsets in locations of torus regions from nominal centrifugal equator. These angular offsets are between the observed locations of these regions and the offset tilted dipole nominal centrifugal equator used in this work. Blue and red symbols show Juno radio occultation results for the cold torus and torus beyond 5.5  $R_J$ , respectively. Circles and triangles represent this work and the work of Phipps et al. (2018); Phipps et al. (2019), respectively. The series of filled circles at intervals of 10° represent the centrifugal equator derived from the (top) JRM09 model with fourth order only and (bottom) combination of the JRM09 model of the internal magnetic field and a model of the magnetic field generated by the magnetospheric current sheet (Phipps et al., 2020). The color of each filled circle indicates distance from Jupiter.

Furthermore, the consistency between the observed Io plasma torus locations and the centrifugal equator locations predicted by a time-independent model demonstrates that the locations of the Io plasma torus, centrifugal equator, and magnetic equator in the inner magnetosphere depend much more strongly on System III longitude than on time. These locations are effectively insensitive to time-varying phenomena in the magnetosphere.

### 7.1.2. Peak TEC

Phipps et al. (2019) found that the peak total electron content of the torus beyond 5.5  $R_J$  did not exhibit any significant variations. They also found that peak total electron content of the cold torus varied considerably, but these variations did not appear to represent a coherent dependence on System III longitude. The smallest value was  $22.2 \pm 2.9$  TECU (PJ6) and the largest value was  $29.3 \pm 2.7$  TECU (PJ1). With the four additional observations provided by PJ10, PJ11, PJ14, and PJ15, we find that the peak total electron content of the torus beyond 5.5  $R_J$  does sometimes vary between observations. The smallest value is  $17.1 \pm 3.5$  TECU (PJ11) and the largest value is  $29.3 \pm 2.7$  TECU (PJ1, still the largest value). However, these variations do not appear to represent a coherent dependence on System III longitude.

Phipps et al. (2019) found that the peak total electron content of the cold torus varied significantly on PJ1–PJ8 from a minimum value of 3.2 TECU to a maximum value of 12.2 TECU. However, the four additional observations of the peak total electron content of the cold torus reported here from PJ10–PJ15 are tightly clustered at 5–7 TECU.

For PJ8 and PJ15, which sampled very similar System III longitudes, the peak total electron contents of the torus beyond  $5.5 R_J$  are within two standard deviations ( $26.7 \pm 2.8$  TECU and  $22.4 \pm 2.9$  TECU, respectively), but the peak total electron contents of the cold torus are quite different ( $12.2 \pm 1.6$  TECU and  $6.31 \pm 1.52$  TECU, respectively). This variability at fixed System III longitude reinforces the earlier conclusion that variations in the peak total electron content of the cold torus do not represent a coherent dependence on System III longitude.

### 7.1.3. Scale Height

Scale height is a proxy for the parallel ion temperature. The scale heights are related to ion temperature, as follows (Phipps & Withers, 2017; Thomas et al., 2004):

$$H = \sqrt{\frac{2k_B T_{\parallel}}{3\Omega^2 \langle M \rangle}} \quad (4)$$

here,  $H$  is the scale height,  $k_B$  is the Boltzmann constant,  $T$  is the parallel ion temperature,  $\Omega$  is the Jupiter rotation rate (corresponding to a period of 9.925 h), and  $\langle M \rangle$  is the mean molecular weight of the ion species in the region of interest (Phipps et al., 2018). This assumes that the mean molecular weight of the torus regions is constant and the temperature in the regions are dominated by the ion temperatures. This does not account for any variability in torus composition. Previous studies have found the composition to be consistent over time and thus we believe this is a reasonable assumption (Bagenal, Dougherty, et al., 2017; Nerney et al., 2017; Thomas et al., 2004). If the electron temperatures are not much less than the ion temperatures (e.g., in the cold torus where ion temperatures are similar to electron temperatures) the temperature is the bulk plasma temperature and not relevant to either electrons or ions. We discuss the variability of the scale height, which is a combination of plasma composition and temperature variability, rather than derive the temperature which requires assumptions about the composition.

Variations in ground-based observations of parallel ion temperature have been discussed by several workers (Brown, 1995; Herbert et al., 2008; Schneider & Trauger, 1995; Schneider et al., 1997). They found that temperatures in the ribbon and in the cold torus varied with System III longitude, and that local time was significant (Herbert et al., 2008). At dawn, both temperatures were smallest around  $60$ – $120^\circ$  System III longitude and greatest around  $200$ – $240^\circ$  System III longitude. At dusk, both temperatures were smallest around  $240^\circ$  System III longitude and greatest around  $30$ – $60^\circ$  System III longitude. Due to their geometry, the Juno radio occultation observations sample a local time around noon.

The scale height of the torus beyond  $5.5 R_J$  does not vary greatly. Six of the eight observed values are within one standard deviation of  $0.94 R_J$ , the seventh is almost within one standard deviation, and the eighth is within two standard deviations. However, there are weak suggestions of possible dependence on System III longitude: values are relatively small at System III longitudes  $50$ – $110^\circ$ , relatively large at System III longitudes  $180$ – $240^\circ$ , and intermediate at other System III longitudes.

The scale height of the cold torus is more variable. The smallest value is  $0.162 \pm 0.011 R_J$  (PJ11) and the largest value is  $0.348 \pm 0.051 R_J$  (PJ1). However, there are weak suggestions of possible dependence on System III longitude: values are relatively small at System III longitudes  $60^\circ$  and  $240^\circ$ , relatively large at System III longitudes  $0^\circ$  and  $180^\circ$ , and intermediate at other System III longitudes.

It should be noted that the weak suggestions of possible dependence of scale height on System III longitude are functionally distinct for the two components of the torus. One peak in System III longitude is suggested for the torus beyond  $5.5 R_J$ , but two peaks in System III longitude are suggested for the cold torus. The ground-based work of Herbert et al. (2008) did not definitively favor either wave-1 or wave-2 dependence on System III longitude. In fact, Herbert et al. (2008) suggested that scale height varies with System III longitude and time. If so, this would complicate the identification of longitudinal trends. Yet scale heights are very similar for PJ8 and PJ15, which sampled very similar System III longitudes. This suggests that scale heights do not depend strongly on time.



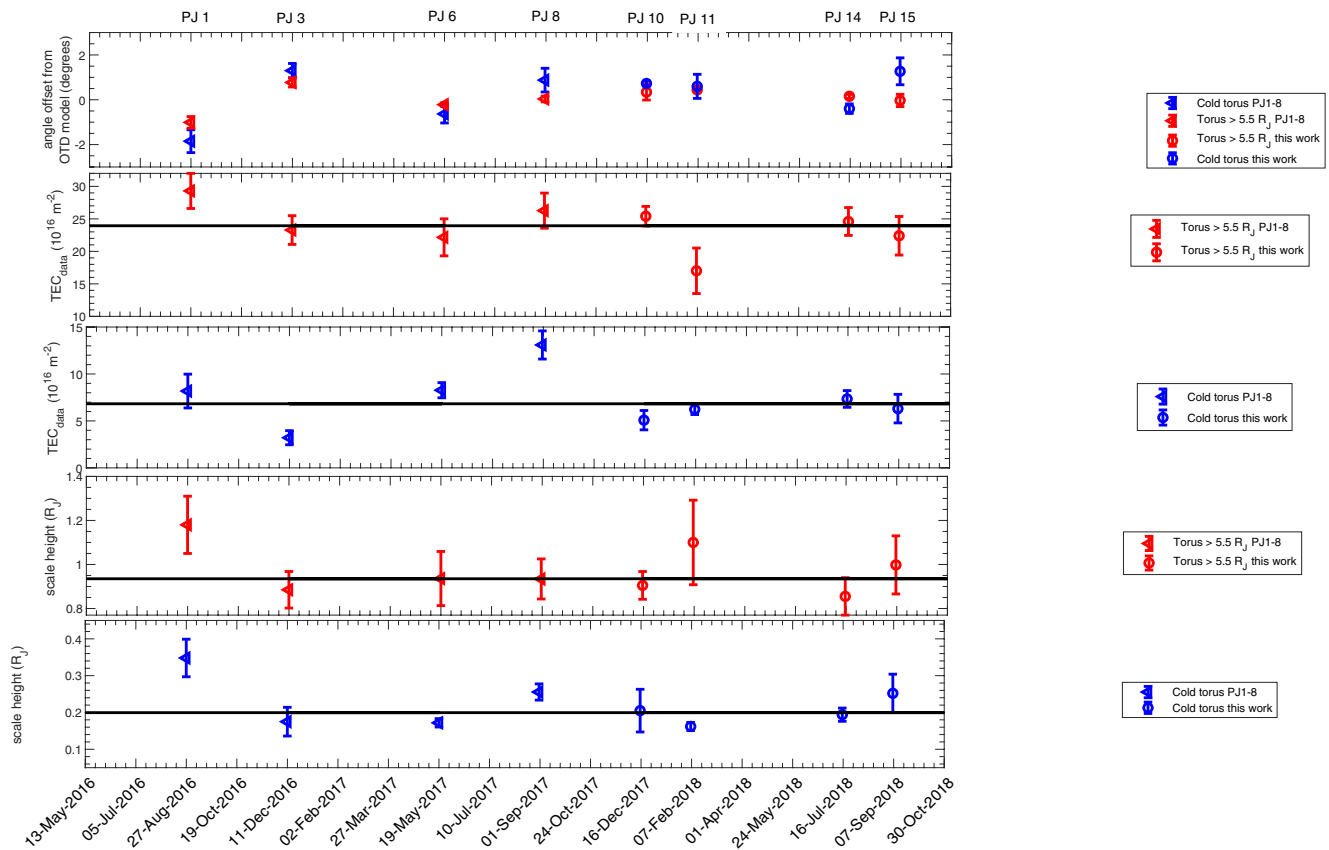


**Figure 13.** (a) Dependence on time of angular offsets in locations of torus regions from nominal centrifugal equator. These angular offsets are between the observed locations of these regions and the offset tilted dipole nominal centrifugal equator used in this work. (b) Dependence on time of fitted peak total electron content of the torus beyond 5.5  $R_J$ . Horizontal lines show the median value of the Juno observations. (c) As panel (b), but for the cold torus. (d) Dependence on time of fitted peak scale height of the torus beyond 5.5  $R_J$ . Horizontal lines show the median value of the Juno observations. (e) As panel (c), but for the cold torus. (all) Blue and red symbols show Juno radio occultation results for the cold torus and torus beyond 5.5  $R_J$ , respectively. Circles and triangles represent this work and the work of Phipps et al. (2019), respectively. The Perijoves are labeled at the top of the figure in plot order from left to right.

## 7.2. Temporal Variability

The Io plasma torus varies with time as well as with longitude. The time between successive Juno Perijoves is approximately 53 days, which determines the timescales to which Juno radio occultation observations of the Io plasma torus are sensitive. The addition of four Perijoves to the earlier results of Phipps et al. (2019) improves the baseline of observations and enhances searches for temporal variability. Figure 13 shows all data from PJ1–PJ15.

### 7.2.1. Angular Tilt

The angular tilts of the two components of the torus do vary but, as shown in Section 7.1.1, these variations are represented well by a dependence on longitude. No additional variations with time are apparent. Note that angular tilt results for PJ1 in the top panel of Figure 14 in Phipps et al. (2019) are shown in the wrong colors: the red symbol should be blue and vice versa. Results for PJ1 in the other panels of Figure 14 in Phipps et al. (2019) are shown correctly.

### 7.2.2. Peak Total Electron Content (TEC)

The observations suggest the possibility of coherent temporal variability in the peak total electron contents of the two components of the torus.

For the torus beyond 5.5  $R_J$ , the peak total electron content decreases as time advances from PJ1 to PJ6 (through PJ3), increases by PJ8, decreases as time advances from PJ8 to PJ11 (through PJ10), increases by

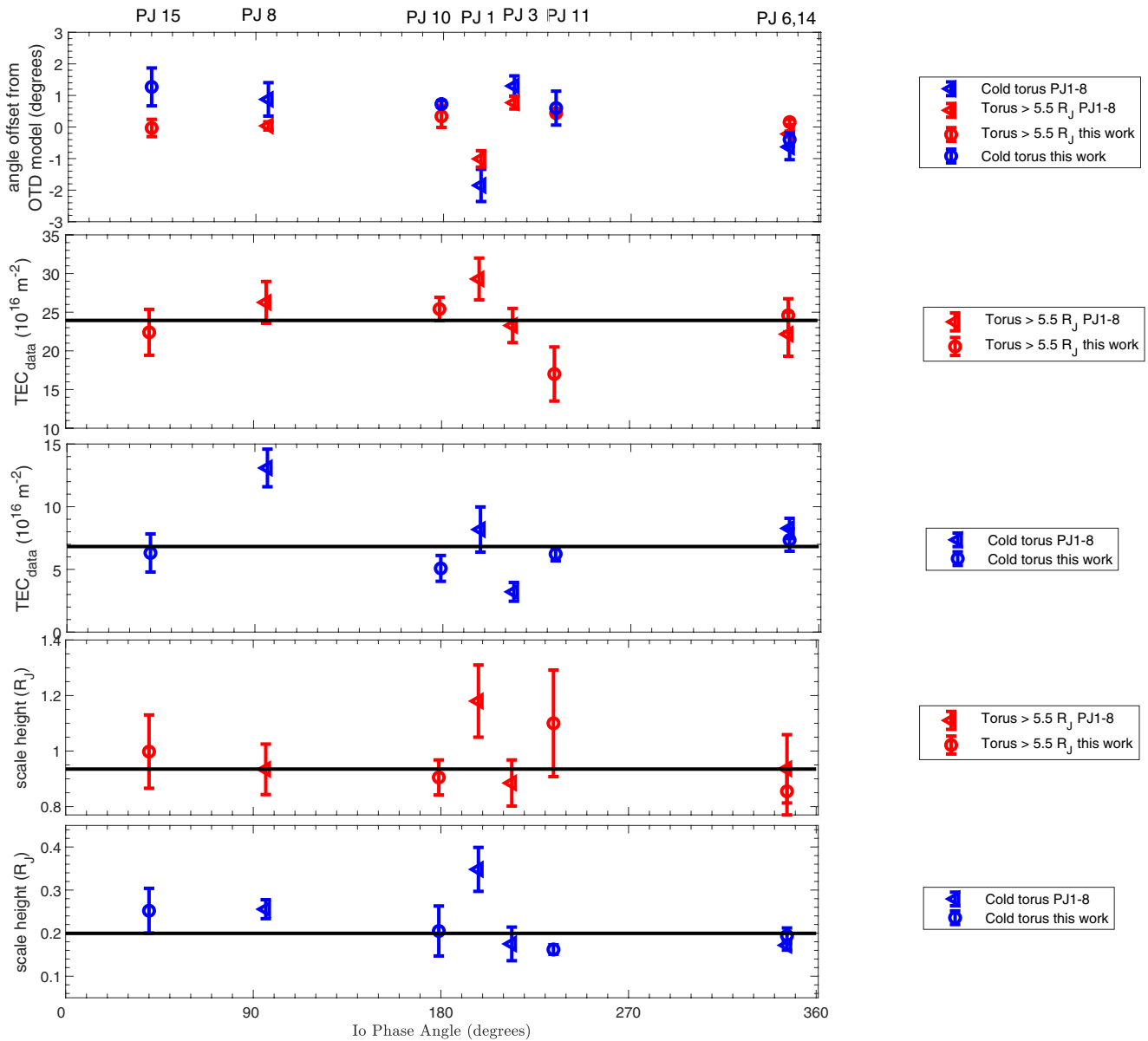


**Figure 14.** (a) Dependence on Io phase angle of angular offsets in locations of torus regions from nominal centrifugal equator. These angular offsets are between the observed locations of these regions and the offset tilted dipole nominal centrifugal equator used in this work. (b) Dependence on Io phase angle of fitted peak total electron content of the torus beyond  $5.5 R_J$ . Horizontal lines show the median value of the Juno observations. (c) As panel (b), but for the cold torus. (d) Dependence on Io phase angle of fitted scale height of the torus beyond  $5.5 R_J$ . Horizontal lines show the median values of the Juno observations. (e) As panel (d), but for the cold torus. (all) Blue and red symbols show Juno radio occultation results for the cold torus and torus beyond  $5.5 R_J$ , respectively. Circles and triangles represent this work and the work of Phipps et al. (2019), respectively. The Perijoves are labeled at the top of the figure in plot order from left to right.

PJ14, and decreases as time advances from PJ14 to PJ15. If the outlier value on PJ11 is set aside, then the peak total electron content decreases steadily and slightly from PJ8 to PJ15.

For the cold torus, the peak total electron content decreases as time advances from PJ1 to PJ3, increases as time advances from PJ3 to PJ8 (through PJ6), decreases as time advances from PJ8 to PJ10, and remains fairly constant as time advances from PJ10 to PJ15 (through PJ11 and PJ14).

In both instances, peak total electron contents rise and fall on timescales that are longer than 30 days and shorter than 300 days. That is, loosely on the order of 100 days. Both peak total electron contents fall from

their PJ1 values, rise to local maxima on PJ8, then settle to more stable behavior from PJ8 to PJ15, if the outlier value for the torus beyond  $5.5 R_J$  on PJ11 is set aside. It is unfortunate that no data are available for PJ4 or PJ5 to address the gap between PJ3 (local minimum in peak total electron content for the cold torus) and PJ6 (local minimum in peak total electron content for the torus beyond  $5.5 R_J$ ).

### 7.2.3. Scale Height

Scale heights in both components of the torus are greatest on PJ1. On subsequent Perijoves, the scale height of the torus beyond  $5.5 R_J$  is smaller but relatively stable. Meanwhile, the scale height of the cold torus increases as time advances from PJ3 to PJ8 (through PJ6), decreases as time advances from PJ8 to PJ11 (through PJ10), and increases as time advances from PJ11 to PJ15 (through PJ14). If the outlier value for the torus beyond  $5.5 R_J$  on PJ11 is set aside, then small variations in the scale height of the torus beyond  $5.5 R_J$  could be consistent with the larger variations seen for the cold torus.

Further observations are needed to discriminate between the competing suggestions of longitudinal and temporal dependencies in the values of torus scale height.

### 7.3. Io Phase Angle

Optical emissions from the Io plasma torus are known to vary with Io phase angle (Volwerk, 2018). As shown in Figure 14, the fitted torus properties determined from Juno radio occultation observations do not show any clear dependence on Io phase angle. Significant variations in fitted torus properties can be seen in the four Perijoves at Io phase angles between  $170^\circ$  and  $250^\circ$ . This suggests that Io phase angle does not significantly influence peak total electron content, scale height, or location of the two fitted components of the torus. However, influences may be more apparent if observations are acquired very close to Io.

### 7.4. All TEC Profiles

Figure 15 shows the dependence of total electron content on distance from the dipolar centrifugal equator for all Perijoves. This illustrates the similarities and differences between observations. The maximum value of total electron content (observed, not fitted) is relatively small at around 25 TECU for PJ3, PJ11, and PJ15, but relatively large at greater than 35 TECU for PJ1 and PJ8. Relatively large scale heights for the torus beyond  $5.5 R_J$  can be seen for PJ1 and PJ11. Asymmetries between the upper and lower sides of the torus can also be seen on PJ8, PJ10, and PJ15.

### 7.5. Comparison Between PJ8 and PJ15

The observation on PJ15 occurred at  $8^\circ$  longitude, very close to the observation 1 year earlier on PJ8 at  $10^\circ$  longitude. These two observations permit a direct test for time variations.

As previously noted in Section 7.1.1, the angular offsets of the two torus components are very similar for these two Perijoves. Furthermore, the scale heights are also very similar. The scale heights for the torus beyond  $5.5 R_J$  are  $0.926 R_J \pm 0.079 R_J$  and  $0.998 R_J \pm 0.132 R_J$  for PJ8 and PJ15, respectively. The scale heights for the cold torus are  $0.231 R_J \pm 0.025 R_J$  and  $0.252 R_J \pm 0.052 R_J$  for PJ8 and PJ15, respectively. Yet the peak total electron content values differ markedly. The peak total electron content values for the torus beyond  $5.5 R_J$  are  $26.7 \pm 2.8$  TECU and  $22.4 \pm 2.9$  TECU for PJ8 and PJ15, respectively. The peak total electron content values for the cold torus are  $12.2 \pm 1.6$  TECU and  $6.31 \pm 1.52$  TECU for PJ8 and PJ15, respectively. The peak total electron content values for the torus beyond  $5.5 R_J$  and the cold torus are greater for PJ8 than for PJ15. These results suggest that scale heights are predominantly influenced by longitude, but peak total electron content values are not.

Figure 16 shows the dependence of total electron content on distance from the dipolar centrifugal equator for these two Perijoves. Clear asymmetries are present between the upper and lower sides of the torus. The shapes of these asymmetries appear similar on these two Perijoves, which is assumed to be due to the similar geometries of the orbits.

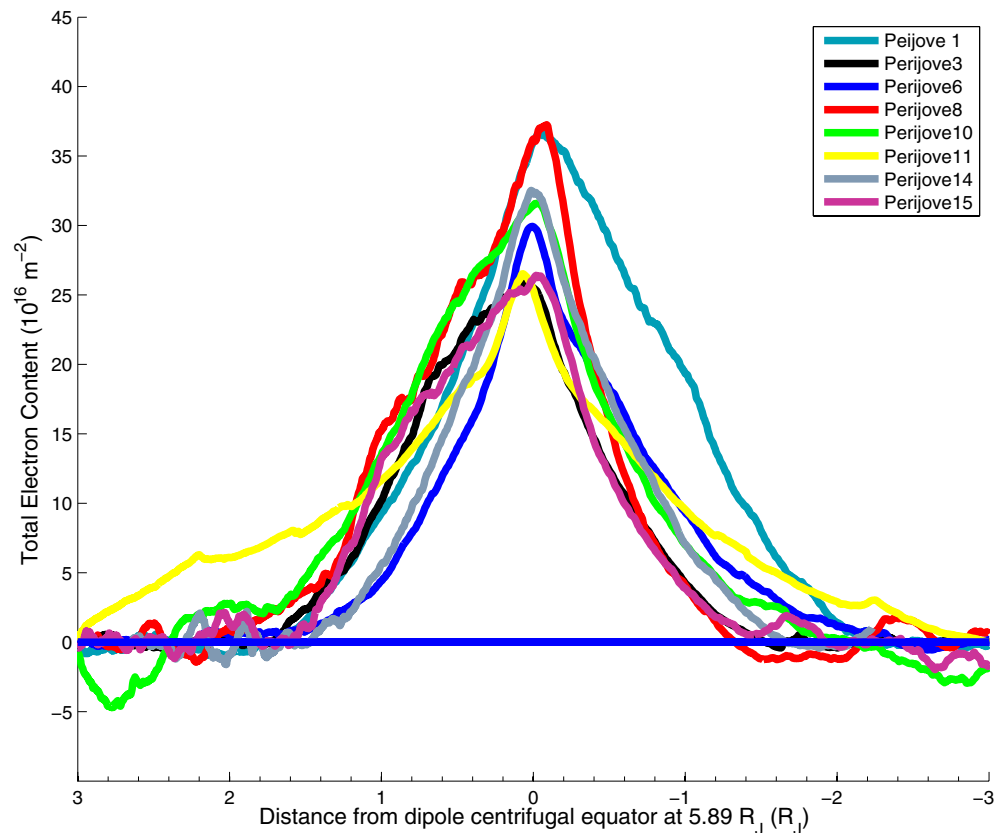


**Figure 15.** Dependence of total electron content measurements from all Perijoves on distance from the dipolar centrifugal equator.

## 8. Summary and Conclusions

Juno conducted gravity observations using two-way X-band and Ka-band observations during Perijoves 10, 11, 14, and 15. These observations used a similar method to that discussed in Phipps et al. (2019). Juno Perijoves 10, 11, 14, and 15 occurred over the span from December 2017 to September 2018. The X-band and Ka-band frequencies received at the Deep Space Network have been used to determine the TEC along the Juno-Earth line of sight during perijove. Correction of the TEC for effects of Earth's ionosphere and a polynomial background trend associated with temporal variations in the solar wind leads to determination of the TEC through the Io plasma torus during a 2 h interval near perijove.

Phipps et al. (2019) previously reported results from analysis of observations from PJ3, PJ6, and PJ8. They found it necessary to apply an ad hoc correction to their data to eliminate trends around perijove that were clearly erroneous. Improved calibrations for ground station delay effects at DSS-25 are now available. Those have been applied to observations from PJ3, PJ6, and PJ8. Application of the improved calibrations has been shown to yield similar results to the ad hoc correction of Phipps et al. (2019), so the results of Phipps et al. (2019) remain valid.

Fits to the total electron content measurements have determined the peak total electron content, scale height, and location of two components of the torus: the cold torus and the torus beyond  $5.5 R_J$ .

The locations of these torus regions can be expressed as angular offsets from the locations expected based on models of the centrifugal equator. Using results from PJ1–PJ8, Phipps et al. (2019) and Phipps et al. (2020) found that these angular offsets vary systematically with longitude. The angular offsets reported here from PJ10–PJ15 agree well with the previously reported systematic dependence on longitude, despite sampling several different longitudes. Furthermore, the angular offsets of the cold torus and the torus beyond  $5.5 R_J$  are distinct. As reported by Phipps et al. (2020), the location of the cold torus is predicted well by a model

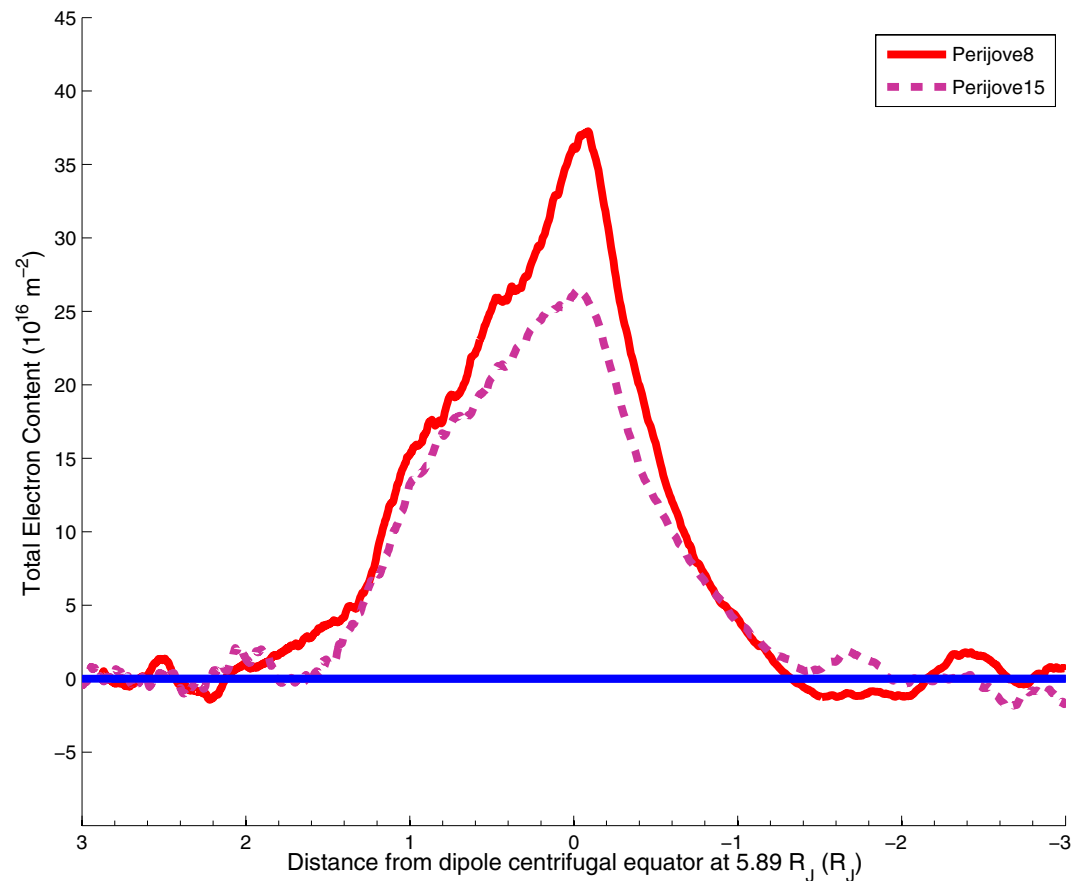


**Figure 16.** Dependence of total electron content measurements from PJ8 (solid line) and PJ15 (dashed line) on distance from the dipolar centrifugal equator.

of Jupiter's internal magnetic field, but prediction of the location of the torus beyond  $5.5 R_J$  requires the addition of contributions from the magnetospheric current sheet. The angular offsets of the cold torus also conform to the picture found from the ground-based observations (Herbert et al., 2008; Schneider & Trauger, 1995). The eight observations analyzed to date do not show any indication of temporal variations in torus location.

The peak total electron content values do not exhibit any clear systematic dependence on longitude. However, there are weak suggestions that these values vary with time on a timescale between 30 and 300 days.

The scale heights of the two torus regions may be weakly dependent on longitude and/or time. The available data do not exclude either hypothesis. In fact, when scale heights are plotted as a function of longitude, they suggest the possibility of longitude dependence, and when scale heights are plotted as a function of time, they suggest the possibility of time dependence. Yet, the suggested longitude dependencies are different for the two torus regions.

Although optical emissions from the Io plasma torus are affected by Io phase angle, the torus properties derived from radio occultation observations do not show any dependence on Io phase angle.

Observations on Perijoves 8 and 15 were acquired at the same longitude 1 year apart. Their angular offsets are consistent, as expected from the finding based upon the full set of observations that angular offsets are predominantly influenced by longitude. Their scale heights are consistent, which suggests that scale heights are also predominantly influenced by longitude. Yet analysis of the full set of observations was unable to exclude either time or longitude as the predominant influence. Additional observations at previously sampled longitudes will resolve whether the agreements between the scale heights of Perijoves 8 and 15 are coincidental or clear indications of the influence of longitude. Their peak total electron content values

are different, as expected from the finding based upon the full set of observations that peak total electron content values are not controlled by longitude.

Analysis of further observations by the Juno spacecraft will clarify the respective roles of longitude, time, and Io phase angle in shaping the density structure of the Io plasma torus. Observations at previously sampled longitudes will be particularly valuable. As the location of the torus beyond  $5.5 R_J$  is affected by magnetospheric currents, more detailed modeling of the centrifugal equator may shed light on conditions in the magnetospheric current sheet at the times of Juno Perijoves.

### Appendix A: Perijoves 10, 11, 14, and 15 Trajectory

Figures 17–20 present the trajectory of the Juno spacecraft during PJ10, PJ11, PJ14, and PJ15, similar to Figure 1 of Phipps et al. (2018) (PJ1) and Appendix A of Phipps et al. (2019) (PJ3, PJ6, and PJ8). This gives an idea of the geometry of the lines of sight used for modeling the occultation on each perijove. For each figure, cylindrical coordinates are used such that the vertical axis shows distance above the plane of the centrifugal equator and the horizontal axis shows distance in the plane of the centrifugal equator. The red disk at the origin shows Jupiter. Black triangles show the position of Juno at 1,000 s intervals. The apparent reversal of Juno's motion at around  $\pm 2 R_J$  above the centrifugal equator is not real; it is an artifact of the chosen coordinate system. Red dashed lines show lines-of-sight from Juno to Earth at the same intervals. The cyan dashed lines indicate the approximate times where the Juno lines of sight pass through the torus. The location of Juno for those lines of sight are indicated with blue circles. The shaded contours show IPT electron densities from Model B of Phipps et al. (2018) (Appendix B). In each figure, the motion of the Juno spacecraft is from the top to the bottom.

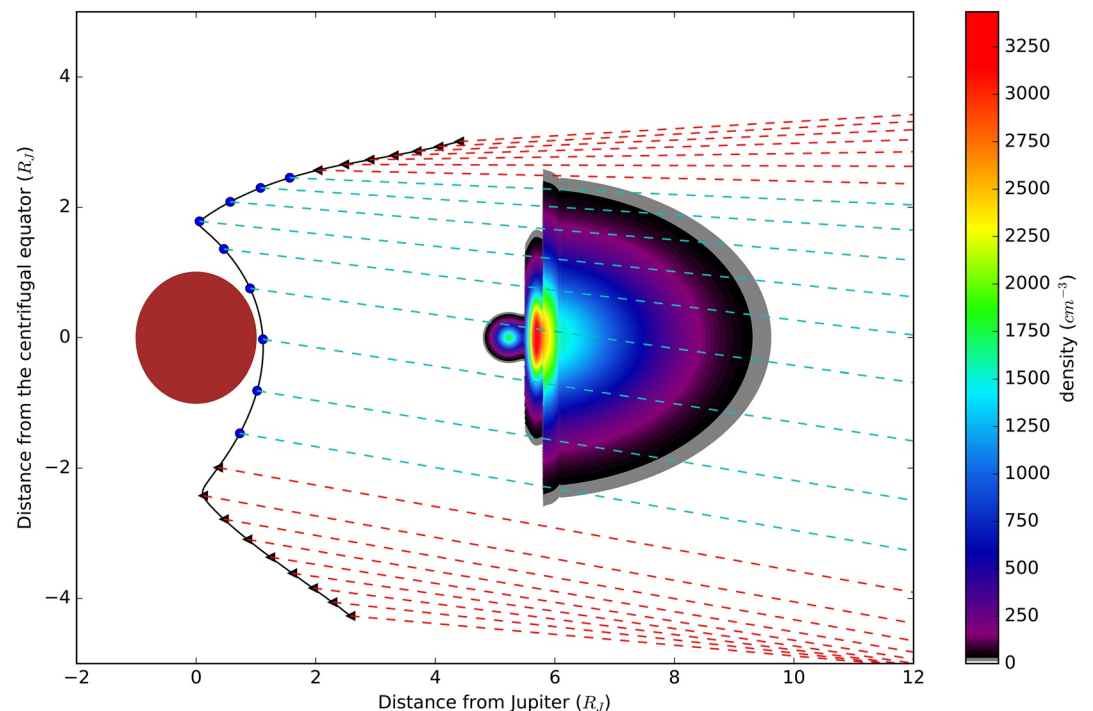


**Figure 17.** Illustration of the geometry of the PJ10 occultation of the Io plasma torus. Centrifugal cylindrical coordinates are used such that the vertical axis shows distance above the plane of the centrifugal equator, and the horizontal axis shows distance in the plane of the centrifugal equator. The red disk at the origin shows Jupiter. Black triangles show the position of Juno at 1,000-s intervals. The apparent reversal of Juno's motion at  $\pm 2 R_J$  above the centrifugal equator is not real; it is an artifact of the chosen coordinate system. Dashed lines show lines of sight from Juno to Earth at the same intervals, with blue color indicating those lines of sight that sample the Io plasma torus. The shaded contours show Io plasma torus electron densities from Model B of Phipps et al. (2018).



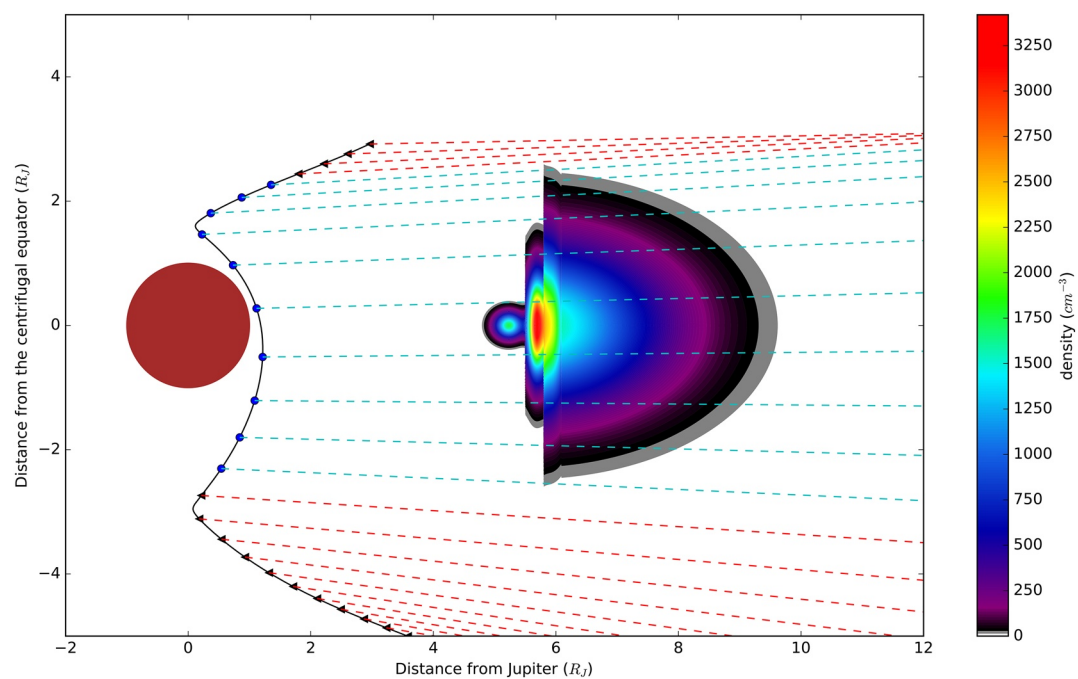


**Figure 18.** As Figure 17, but for PJ11.

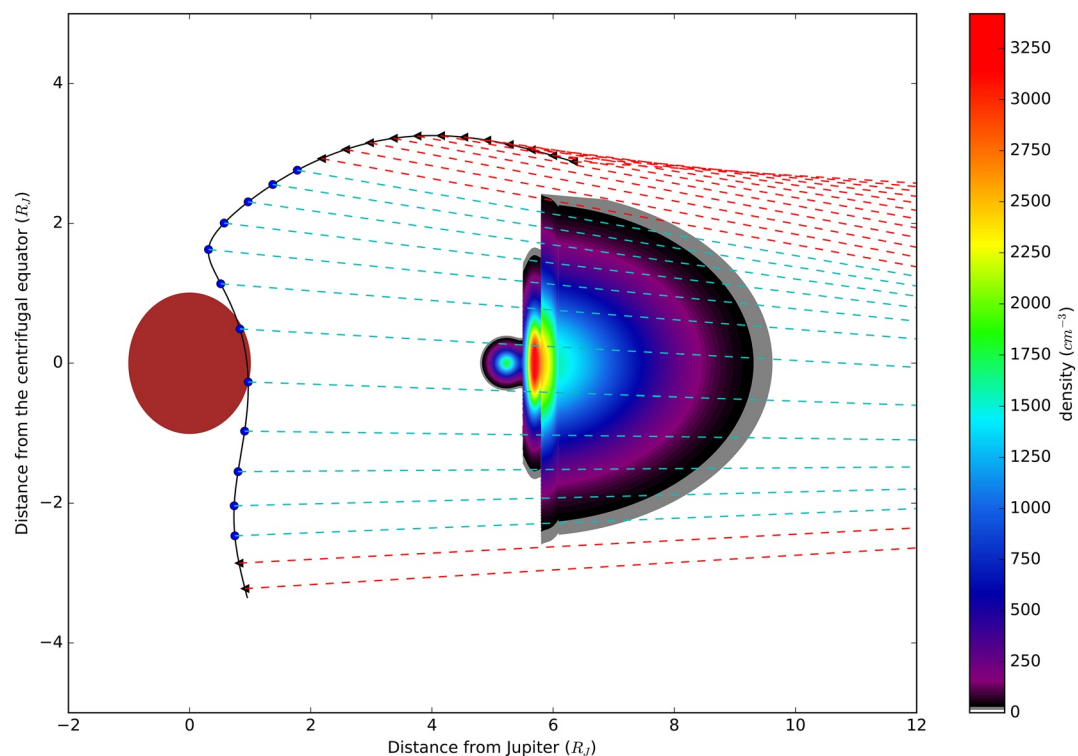


**Figure 19.** As Figure 17, but for PJ14.

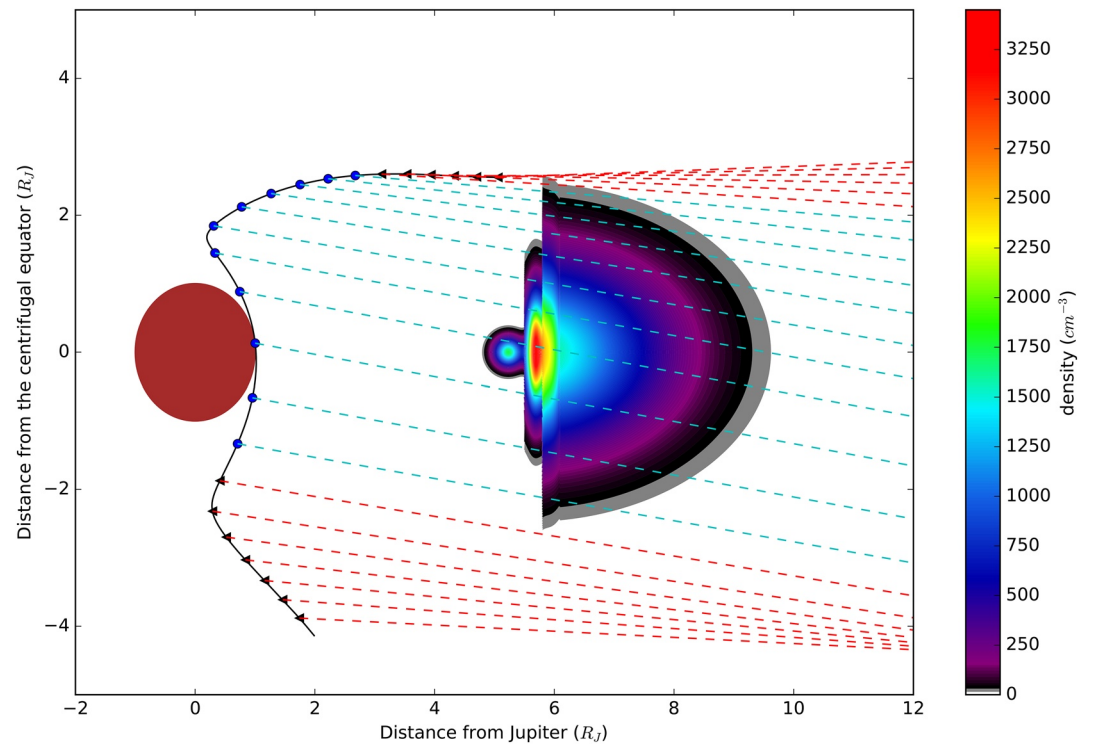


**Figure 20.** As Figure 17, but for PJ15.

## Appendix B: Parameters of Model B of Phipps et al. (2018)

The density distribution used in this paper was introduced and discussed in detail in Phipps and Withers (2017). Model parameters were updated in Model B of Phipps et al. (2018). The equations for the distribution are:

$$N(R < 6.1R_J, r) = N_1 e^{-\frac{(R-C_1)^2}{(w_1)^2} - \frac{r^2}{H_1^2}} + N_2 e^{-\frac{(R-C_2)^2}{(w_2)^2} - \frac{r^2}{H_2^2}} + N_3 e^{-\frac{(R-C_3)^2}{(w_3)^2} - \frac{r^2}{H_3^2}} \quad (\text{B.1})$$

$$N(R > 6.1R_J, r) = N_4 e^{-\frac{(R-C_4)^2}{(w_4)^2} - \frac{r^2}{H_4^2}}. \quad (\text{B.2})$$

here,  $r$  is the distance perpendicular to the centrifugal equator,  $R$  is the radial distance from Jupiter,  $N_n$  is the central reference density,  $C_n$  is the radial peak location,  $W_n$  is the radial width of each region ( $0.2 R_J$  for the cold torus,  $0.32 R_J$  for ribbon,  $0.32 R_J$  for warm torus, and  $1.88 R_J$  for extended torus Gaussian), and  $H_n$  is the scale height. 1 refers to the cold torus, 2 to the ribbon, 3 to the warm torus, and four to an extended torus used to match the data beyond  $6.1 R_J$ . The numerical values of the parameters of Model B are shown in Table 1 in Phipps et al. (2018).

## Data Availability Statement

The raw gravity science data used in this work are publicly available on the NASA Planetary Data System at [http://pds-atmospheres.nmsu.edu/data\\_and\\_services/atmospheres\\_data/JUNO/gravity.html](http://pds-atmospheres.nmsu.edu/data_and_services/atmospheres_data/JUNO/gravity.html). The data used in this manuscript are available at <https://doi.org/10.5281/zenodo.4020746>.

## Acknowledgments

The authors would like to thank the three anonymous referees for their reviews of this manuscript. The work of D. Buccino, M. Parisi, and O. Yang was carried out at the Jet Propulsion Laboratory, California Institute of Technology, under a contract with the National Aeronautics and Space Administration. Government sponsorship acknowledged. This work was supported in part by NASA award 80NSSC19K0818.

## References

- Asmar, S. W., Bolton, S. J., Buccino, D. R., Cornish, T. P., Folkner, W. M., Formaro, R., et al. (2017). The Juno gravity science instrument. *Space Science Reviews*, 213, 205–218. <https://doi.org/10.1007/s11214-017-0428-7>
- Bagenal, F. (1994). Empirical model of the Io plasma torus: Voyager measurements. *Journal of Geophysical Research*, 99, 11043–11062. <https://doi.org/10.1029/93JA02908>
- Bagenal, F., Adriani, A., Allegrini, F., Bolton, S. J., Bonfond, B., Bunce, E. J., et al. (2017a). Magnetospheric science objectives of the Juno mission. *Space Science Reviews*, 213, 219–287. <https://doi.org/10.1007/s11214-014-0036-8>
- Bagenal, F., Dougherty, L. P., Bodisch, K. M., Richardson, J. D., & Belcher, J. M. (2017b). Survey of Voyager plasma science ions at Jupiter: 1. Analysis method. *Journal of Geophysical Research*, 122, 8241–8256. <https://doi.org/10.1002/2016JA023797>
- Bagenal, F., & Sullivan, J. D. (1981). Direct plasma measurements in the Io torus and inner magnetosphere of Jupiter. *Journal of Geophysical Research*, 86, 8447–8466. <https://doi.org/10.1029/JA086iA10p08447>
- Brown, M. E. (1995). Periodicities in the Io plasma torus. *Journal of Geophysical Research*, 100, 21683–21696. <https://doi.org/10.1029/95JA01988>
- Buccino, D. R. (2016). *Juno Jupiter gravity science raw data set V1.0, JUNO-JRSS-1-JUGR-V1.0, NASA planetary data system, pds-atmospheres.nmsu.edu/data\_and\_services/atmospheres\_data/JUNO/gra-vity.html*.
- Buccino, D. R., Border, J., Volk, C., & Yang, O. (2019). Measurement of station delay at DSS-25. *The Interplanetary Network Progress Report*, 42–217, 1–11. Retrieved from [https://ipnpr.jpl.nasa.gov/progress\\_report/42-217/42-217B.pdf](https://ipnpr.jpl.nasa.gov/progress_report/42-217/42-217B.pdf)
- Connerney, J. E. P., Acuna, M. H., & Ness, N. F. (1981). Modeling the Jovian current sheet and inner magnetosphere. *Journal of Geophysical Research*, 86, 8370–8384. <https://doi.org/10.1029/JA086iA10p08370>
- Connerney, J. E. P., Kotsiaros, S., Oliverson, R. J., Espley, J. R., Joergensen, J. L., Joergensen, P. S., et al. (2018). A new model of Jupiter's magnetic field from Juno's first nine orbits. *Geophysical Research Letters*, 45, 2590–2596. <https://doi.org/10.1002/2018GL077312>
- Cummings, W., Dessler, A., & Hill, T. (1980). Latitudinal oscillations of plasma within the Io torus. *Journal of Geophysical Research*, 85, 2108–2114. <https://doi.org/10.1029/JA085iA05p02108>
- Durante, D., Parisi, M., Serra, D., Zannoni, M., Notaro, V., Racioppa, P., et al. (2020). Jupiter's gravity field halfway through the Juno mission. *Geophysical Research Letters*, 47, e2019GL086. <https://doi.org/10.1029/2019GL086572>
- Foreman-Mackey, D., Hogg, D. W., Lang, D., & Goodman, J. (2013). emcee: The MCMC hammer. *Publications of the Astronomical Society of the Pacific*, 125, 306–312. <https://doi.org/10.1086/670067>
- Herbert, F., Schneider, N. M., & Dessler, A. J. (2008). New description of Io's cold plasma torus. *Journal of Geophysical Research*, 113, A01208. <https://doi.org/10.1029/2007JA012555>
- Khurana, K. K., Kivelson, M. G., Vasyliunas, V. M., Krupp, N., Woch, J., Lagg, A., et al. (2004). *The configuration of Jupiter's magnetosphere*. Cambridge, UK: Cambridge University Press, 593–616.
- Mariotti, G., & Tortora, P. (2013). Experimental validation of a dual uplink multifrequency dispersive noise calibration scheme for Deep Space tracking. *Radio Science*, 48, 111–117. <https://doi.org/10.1002/rds.20024>
- Nerney, E. G., Bagenal, F., & Steffl, A. J. (2017). Io plasma torus ion composition: Voyager, Galileo, and Cassini. *Journal of Geophysical Research*, 122, 727–744. <https://doi.org/10.1002/2016JA023306>
- Nozawa, H., Misawa, H., Kagitani, M., Tsuchiya, F., Takahashi, S., Morioka, A., et al. (2006). Implication for the solar wind effect on the Io plasma torus. *Geophysical Research Letters*, 33, L16103. <https://doi.org/10.1029/2005GL025623>
- Nozawa, H., Misawa, H., Takahashi, S., Morioka, A., Okano, S., & Sood, R. (2004). Long-term variability of [SII] emissions from the Io plasma torus between 1997 and 2000. *Journal of Geophysical Research*, 109, A07209. <https://doi.org/10.1029/2003JA010241>
- Nozawa, H., Misawa, H., Takahashi, S., Morioka, A., Okano, S., & Sood, R. (2005). Relationship between the Jovian magnetospheric plasma density and Io torus emission. *Geophysical Research Letters*, 32, L11101. <https://doi.org/10.1029/2005GL022759>
- Parisi, M., Buccino, D. R., & Yang, Y.-M. (2018). *Plasma noise calibration of two-way Doppler data*. Pasadena, CA: Jet Propulsion Laboratory Interoffice Memorandum, 332-DRB-20181018-19.
- Phipps, P. H., & Withers, P. (2017). Radio occultations of the Io plasma torus by Juno are feasible. *Journal of Geophysical Research*, 122, 1731–1750. <https://doi.org/10.1002/2016JA023447>
- Phipps, P. H., Withers, P., Buccino, D. R., Yang, Y.-M., & Parisi, M. (2019). Variations in the density distribution of the Io plasma torus as seen by radio occultations on Juno perijoves 3, 6, and 8. *Journal of Geophysical Research: Space Physics*, 124, 5200–5221. <https://doi.org/10.1029/2018JA026297>
- Phipps, P. H., Withers, P., Vogt, M. F., Buccino, D. R., Yang, Y.-M., Parisi, M., et al. (2020). Where is the Io plasma torus? A comparison of observations by Juno radio occultations to predictions from Jovian magnetic field models. *Journal of Geophysical Research: Space Physics*, 125. <https://doi.org/10.1029/2019JA027633>
- Phipps, P. H., Withers, P., Buccino, D. R., & Yang, Y.-M. (2018). Distribution of plasma in the Io plasma torus as seen by radio occultation during Juno Perijove 1. *Journal of Geophysical Research*, 123, 6207–6222. <https://doi.org/10.1029/2017JA025113>
- Schmidt, C., Schneider, N., Leblanc, F., Gray, C., Morgenthaler, J., Turner, J., & Grava, C. (2018). A survey of visible S<sup>+</sup> emission in Io's plasma torus during the hisaki epoch. *Journal of Geophysical Research: Space Physics*, 123, 5610–5624. <https://doi.org/10.1029/2018JA025296>
- Schneider, N. M., Taylor, M. H., Cray, F. J., & Trauger, J. T. (1997). On the nature of the  $\lambda_{\text{III}}$  brightness asymmetry in the Io torus. *Journal of Geophysical Research*, 102, 19823–19834. <https://doi.org/10.1029/97JA00773>
- Schneider, N. M., & Trauger, J. T. (1995). The Structure of the Io Torus. *The Astrophysical Journal*, 450, 450. <https://doi.org/10.1086/176155>
- Steffl, A. J., Bagenal, F., & Stewart, A. I. F. (2004b). Cassini UVIS observations of the Io plasma torus. II. Radial variations. *Icarus*, 172, 91–103. <https://doi.org/10.1016/j.icarus.2004.04.016>
- Steffl, A. J., Delamere, P. A., & Bagenal, F. (2006). Cassini UVIS observations of the Io plasma torus. III. Observations of temporal and azimuthal variability. *Icarus*, 180, 124–140. <https://doi.org/10.1016/j.icarus.2005.07.013>
- Steffl, A. J., Delamere, P. A., & Bagenal, F. (2008). Cassini UVIS observations of the Io plasma torus. IV. Modeling temporal and azimuthal variability. *Icarus*, 194, 153–165. <https://doi.org/10.1016/j.icarus.2007.09.019>
- Steffl, A. J., Stewart, A. I. F., & Bagenal, F. (2004a). Cassini UVIS observations of the Io plasma torus. I. Initial results. *Icarus*, 172, 78–90. <https://doi.org/10.1016/j.icarus.2003.12.027>
- Thomas, N., Bagenal, F., Hill, T. W., & Wilson, J. K. (2004). The Io neutral clouds and plasma torus. In F. Bagenal, T. E. Dowling, & W. B. McKinnon (Eds.), *Jupiter: The planet, satellites and magnetosphere*. (pp. 561–591). Cambridge, UK: Cambridge University Press.
- Tsuchiya, F., Arakawa, R., Misawa, H., Kagitani, M., Koga, R., Suzuki, F., et al. (2019). Azimuthal variation in the Io plasma torus observed by the hisaki satellite from 2013 to 2016. *Journal of Geophysical Research*, 124. <https://doi.org/10.1029/2018JA026038>

- Tsuchiya, F., Kagitani, M., Yoshioka, K., Kimura, T., Murakami, G., Yamazaki, A., et al. (2015). Local electron heating in the Io plasma torus associated with Io from HISAKI satellite observation. *Journal of Geophysical Research*, *120*, 10317–10333. <https://doi.org/10.1002/2015JA021420>
- Vasyliunas, V. M. (1983). *Plasma distribution and flow*. Cambridge, UK: Cambridge University Press. 395–453
- Volwerk, M. (2018). On the location of the Io plasma torus: Voyager 1 observations. *Annales Geophysicae*, *36*, 831–839. <https://doi.org/10.5194/angeo-36-831-2018>
- Yoneda, M., Kagitani, M., & Okano, S. (2009). Short-term variability of Jupiter's extended sodium nebula. *Icarus*, *204*, 589–596. <https://doi.org/10.1016/j.icarus.2009.07.023>
- Yoneda, M., Nozawa, H., Misawa, H., Kagitani, M., & Okano, S. (2010). Jupiter's magnetospheric change by Io's volcanoes, *Geophysical Research Letters*, *37*, L11202. <https://doi.org/10.1029/2010GL043656>
- Yoneda, M., Tsuchiya, F., Misawa, H., Bonfond, B., Tao, C., Kagitani, M., & Okano, S. (2013). Io's volcanism controls Jupiter's radio emissions. *Geophysical Research Letters*, *40*, 671–675. <https://doi.org/10.1002/grl.50095>